Regionally divergent drivers behind transgressions of the freshwater change planetary boundary

Vili Virkki[1,*], Lauren Seaby Andersen[2], Sofie te Wierik[2], Dieter Gerten[2,3,4], Miina Porkka[1]

[1] Department of Environmental and Biological Sciences, University of Eastern Finland, Joensuu, Finland
[2] Potsdam Institute for Climate Impact Research, Member of the Leibniz Association, Potsdam, Germany
[3] Geography Department, Humboldt-Universität zu Berlin, Berlin, Germany
[4] Integrative Research Institute on Transformations of Human-Environment Systems, Humboldt-Universität zu Berlin, Berlin, Germany

* Corresponding author. E-mail: vili.virkki@uef.fi

Abstract

Human-driven freshwater change contributes to elevated Earth system risks. Here, we advance the understanding of drivers behind the transgression of the planetary boundary for freshwater change (PB-FW), based on historical (1901–2019) streamflow (blue water) and soil moisture (green water) simulations from a large ensemble of global hydrological models. Since the former estimate ending in 2005, PB-FW transgression has increased across its blue and green water components. Decomposition of climate-related forcing and direct human forcing (encompassing land and water use changes) shows that climate has increasingly become the dominant global influence on dry and wet streamflow and soil moisture deviations from preindustrial-like conditions. Moreover, direct human forcings intensify particularly dry deviations in regions with compounding pressures on ecosystems. Our approach characterises the main drivers of blue and green water changes in regional hotspots, improving the utility of the PB-FW for guiding mitigation and adaptation strategies in response to freshwater change.

Main

Freshwater plays an integral role in the functioning of the Earth system[1]. Human activities, however, continue to modify the freshwater cycle, by direct water withdrawals and flow regulation, and through anthropogenic climate and land cover change, for instance[2–5], contributing to risks of Earth system disruptions. As freshwater is deeply connected to ecological processes, anomalous hydrological conditions – including increased frequency and magnitude of drying or wetting across water cycle elements – can destabilise ecosystems where freshwater availability governs their resilience[6–8]. Moreover, freshwater change modifies climatic processes by, for instance, altering land-atmosphere carbon exchange[9,10] and moisture recycling[11,12], often in a teleconnected manner that propagates impacts beyond their origin and across scales[13,14]. Although thresholds for adverse impacts of freshwater change can be case-specific and uncertain[15], deviations from historically stable hydrological conditions are likely associated with increasing risks of both abrupt and gradual ecological and climatic impacts[16,17].

The planetary boundaries (PBs) framework aims for understanding and assessing multiple anthropogenic perturbations to the Earth system and their risks to vitally important Earth system processes[18]. The recently updated PB for freshwater change (PB-FW) builds on the premise that increasingly frequent anomalous hydrological conditions serve as indicators of broader stress on freshwater's Earth system functions[16,17]. The PB-FW is shown to be notably transgressed, which marks an elevated level of Earth system risks due to freshwater change[18]. Unlike earlier approaches based on global human water consumption, calculated top-down based on global consumption[19] or bottom-up based on regional appropriation of rivers' environmental flow requirements[20,21], the new PB-FW integrates the evolution of both blue water (streamflow) and green water (soil moisture) changes in a consistent assessment scheme. It allows for spatial disaggregation of the PB-FW, offering a globally coherent evaluation considering regional patterns of change. The PB-FW thus provides a valuable conceptual foundation for understanding human-driven freshwater change.

The recent PB-FW analysis[16] identified broad change patterns across global, regional and local scales but did not quantitatively explore historical drivers of the PB-FW transgression trajectory. Moreover, the last two decades of global hydrological change were not represented in the analysis with data spanning only until 2005. It is important to consider those gaps because drivers and impacts of freshwater change vary widely across space and time[5,22–26], and recent decades have shown intense change in the freshwater cycle[2,27–29]. Addressing these gaps using the newly proposed PB-FW methodology is essential to link the PB-FW metrics to regional drivers of freshwater change, which ultimately cause the hydrologic anomalies that underlie the globally aggregated PB-FW transgression. Having this knowledge, the PB-FW and the PBs framework can better be utilised for mitigating or adapting to Earth system risks related to freshwater change[30–32].

In this study, we isolate major historical drivers of the global PB-FW transgression trajectory and analyse their regional decomposition. First, we reassess the currently available state-of-the-art PB-FW analysis and extend it to the year 2019, adding 15 years to the previous estimate[16], using a large ensemble of updated hydrological model simulations. We then decompose the historical contributions of direct human forcing (DHF; including water use and land cover change, for instance) and climate-related forcing (CRF) to PB-FW metrics at global and regional scales, which advances from previous analysis. Our approach provides an attribution of drivers of the hydrological change underlying the PB-FW and identifies regions that contribute to freshwater-related risks in the Earth system given their historical dependencies and impacts on blue and green water resources.

Reassessing the planetary boundary for freshwater change

The methodological framework of this study remains consistent with the newest PB-FW definition[16]. We first established local variability bounds for both streamflow and soil moisture at the grid cell scale (between local 5^{th}–95^{th} percentiles) under a baseline scenario that is largely undisturbed by human actions (Methods). Subsequently, we determined local deviations – i.e. events of anomalously dry and wet streamflow or soil moisture conditions falling outside of the 5^{th}–95^{th} percentile range – and estimated the occurrence of these deviations by aggregating them to the percentage of global or regional land area with local deviations (Methods). Variability in the occurrence of local deviations under the baseline scenario was finally used to set two reference boundaries at the global scale and within each region: one at the median of baseline variability and one at the upper end (95^{th} percentile) of baseline variability (Methods). At the global scale, the upper end reference boundary corresponds to the PB-FW[16].

We employed an updated, maximally large ensemble of state-of-the-art global hydrological models (GHMs) from the Inter-Sectoral Impact Model Intercomparison Project (ISIMIP) simulation round 3a[33,34]. The data cover years 1901–2019 and are simulated using reanalysis-based climate-related forcing (CRF) together with dynamic direct human forcing (DHF). To establish the baseline conditions, we used counterfactual simulations that assumed fixed DHF at 1901 levels and, respectively, CRF derived from detrended historical climate reanalysis data (Methods). We attributed hydrological changes to CRF and DHF by a scenario comparison, which is a generic attribution approach that has commonly been used in global water cycle change research[2,25]. In this approach, the historical scenario, as well as hypothetical CRF only and DHF only scenarios, were compared to the counterfactual baseline scenario; differences to the baseline scenario were defined as scenario contributions (Methods).

Historical CRF and DHF contributions on PB-FW

The degree of PB-FW transgression has increased for both streamflow and soil moisture during the past two decades (Fig. 1). Local deviations during the last decade of our analysis (mean of 2010–2019)

affected 22.6% of the global ice-free land area for streamflow (~29.4 million km^2) and 22.0% for soil moisture (~28.6 million km^2). These figures are 75% and 77% higher than the upper end of baseline variability that represents the PB-FW, which is 12.9% and 12.4% for streamflow and soil moisture, respectively (Fig. 1). This reassessment suggests that the previous PB-FW status estimate[16] may have been conservative; at the endpoint of the previous estimate in 2005, our new estimate is 2–3 percentage points (pp) higher compared to the previous estimate (18.2% & 15.8%; Fig. 1). Relative to the PB at the upper end of baseline variability, however, these differences appear not equally large because the reassessment places the PB-FW at 12.4–12.9% (Fig. 1), whereas the previous estimate placed it around 10–11%[16].

Based on the reassessment, PB-FW was persistently transgressed at around the 1940s (Fig. 1), after which the freshwater cycle has increasingly deviated from the baseline conditions with little sign of stabilisation. On average, during 1990–2019, the global land area affected by local streamflow and soil moisture deviations has increased with a rate of 0.18 pp/year and 0.22 pp/year, respectively (Methods). These rates indicate increasingly severe PB-FW transgression and elevated freshwater-related risks in the Earth system.

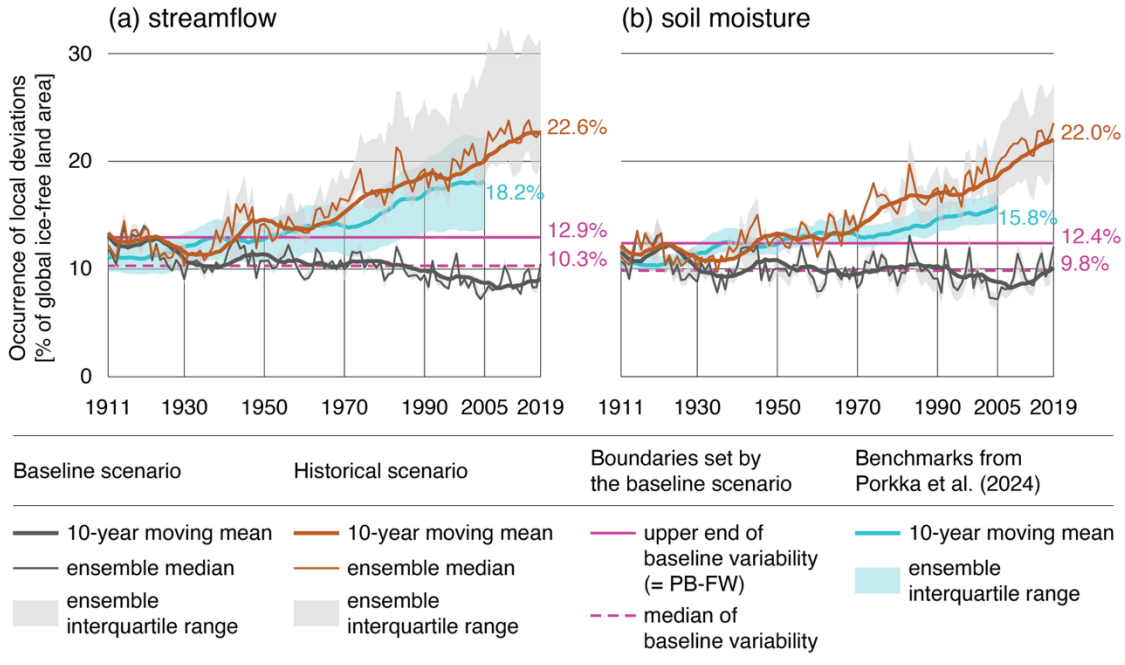

Figure 1. Global occurrence of local deviations. The global occurrence of local deviations is measured by the percentage share of global ice-free land area with dry and wet local deviations, for streamflow (a) and soil moisture (b). Shown is the ensemble median of annual percentage, which is computed as an average of monthly percentages (Methods). The occurrence of local deviations in 2019 (mean of 2010–2019) marks the current status of the planetary boundary for freshwater change (PB-FW). The baseline and historical scenario ensemble median and ensemble interquartile range are computed from n = 12 (streamflow) and n = 4 (soil moisture) ensemble members (Methods). Benchmark values until year 2005 are taken from the previous PB-FW status estimate[16].

Dry deviations are more widespread compared to wet deviations for both streamflow and soil moisture (Fig. 2c–f). However, local deviation occurrence in all four subcomponents of the PB-FW (i.e. dry and wet deviations, streamflow and soil moisture) show more than a doubling compared to the median of baseline variability that depicts a typical deviation occurrence value under baseline conditions (Fig. 2c–f). Between 1990–2019, the occurrence of dry streamflow and soil moisture deviations increased at the fastest rates (0.13 pp/yr; 0.21 pp/yr, respectively) (Fig. 2c, e), while wet streamflow and soil moisture deviations increased at more gradual rates (0.078 pp/yr; 0.064 pp/yr, respectively) (Fig. 2d, f). Additionally, the increasing trajectories in dry deviation occurrence (Fig. 2c, e) appear slightly less smooth compared to wet deviation occurrences (Fig. 2d, f), which may suggest larger interannual variance in dry deviations.

Differences in the analysed hydrological model ensembles (Methods) are apparent in how our estimates differ from the previously reported global PB-FW status[16] since the mid-20th century. Local deviations are now found to occupy larger areas; for year 2005, local deviation occurrence in all four subcomponents places at around 10% (Fig. 2c–f), which generally signifies increases from previously reported dry and wet streamflow and soil moisture deviation occurrences between 6–10%[16]. These differences stem from the updated selection of hydrological models and particularly climate forcings (Methods), which show increased wet streamflow deviations when comparing against the previous PB-FW estimate (Supplementary Fig. 1) and notable variation between each other (Supplementary Fig. 1–4). Moreover, although the baseline scenario uses detrended climate forcing based on reanalysis data (Methods), slight residual trends downwards are visible in the baseline scenario, especially for streamflow deviations (Fig. 1–2). While these differences serve as an important reminder of the dependency of PB-FW assessments on model ensemble selection, the broad trend of increasing PB-FW transgression across its subcomponents is clearly distinguishable and robust.

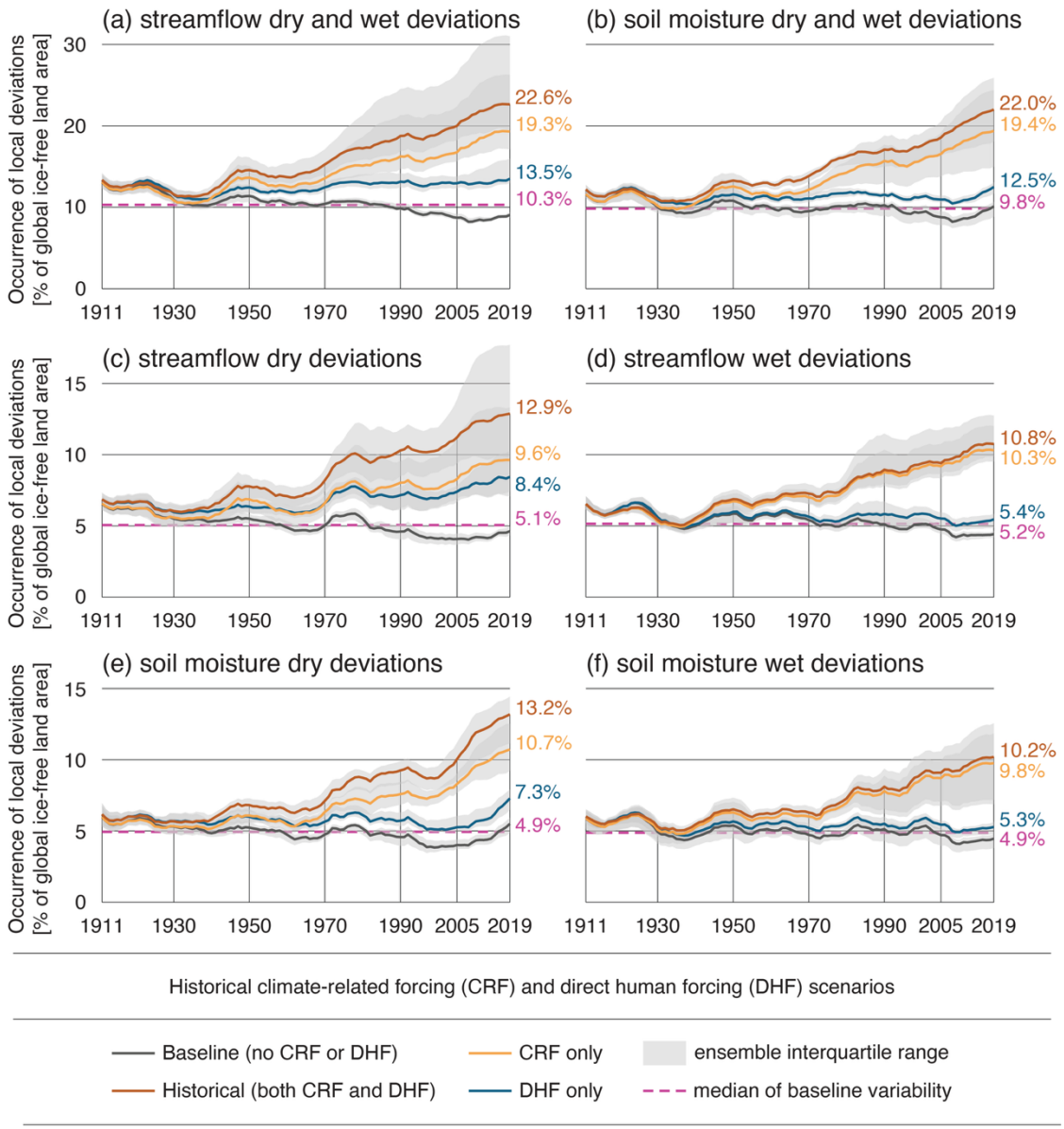

Figure 2. Global occurrence of dry and wet local deviations under different climate-related forcing and direct human forcing scenarios. The global occurrence of local deviations is measured by the percentage share of global ice-free land area with local deviations, for dry and wet streamflow deviations (a), dry and wet soil moisture deviations (b), dry streamflow deviations (c), wet streamflow deviations (d), dry soil moisture deviations (e), and wet soil moisture deviations (f). The baseline and historical scenarios in panels a and b correspond to Fig. 1a and Fig. 1b, respectively. Shown is the ensemble median of annual percentage, which is computed as an average of monthly percentages (Methods). Time series of the occurrence of local deviations and limits of the ensemble interquartile range (IQR) are smoothed with a 10-year moving (trailing) mean over the ensemble median and ensemble IQR limits, respectively.

At the global scale, CRF is the primary driver of PB-FW transgression (Fig. 2a–b), though its degree of dominance varies over time as well as across dry and wet streamflow and soil moisture deviations (Fig. 2c–f). CRF is almost fully responsible for increases in wet streamflow and soil moisture deviations (Fig. 2d, f), while dry deviations reflect a more mixed influence from both CRF and DHF (Fig. 2c, e). Globally, the influence of DHF is to amplify dry deviations; without DHF, dry deviation occurrence would be like wet deviation occurrence, but with both CRF and DHF included, dry deviation occurrence

is higher compared to wet deviation occurrence (Fig. 2c, e). The divergence between CRF only and DHF only scenarios begins to notably widen around the 1970s for all other components except for dry streamflow deviations, which shows how the impact of climate change has become more pronounced in the freshwater cycle during the late 20th and early 21st century (Fig. 2d–f).

Regional occurrence of local deviations

In addition to global PB-FW patterns (Fig. 1–2), it is essential to identify and distinguish the regional drivers of the underlying changes, since each distinct region of the world follows its unique trajectory of streamflow and soil moisture deviations. We used the HydroBASINS level 4 catchment delineation[35] to assess these trajectories and to disaggregate the global PB-FW transgression into regional components (Methods). This regional analysis mirrors the global method: we established local bounds under baseline conditions, estimated the regional occurrence of local deviations for the four different scenarios and finally set region-specific (PB-like) reference boundaries at the median and upper end of baseline variability (Fig. 3a, Methods). To allow comparison between regions with different levels of natural variation in local deviations, we normalised the regional occurrence of local deviations relative to these two reference boundaries (Fig. 3a, Methods).

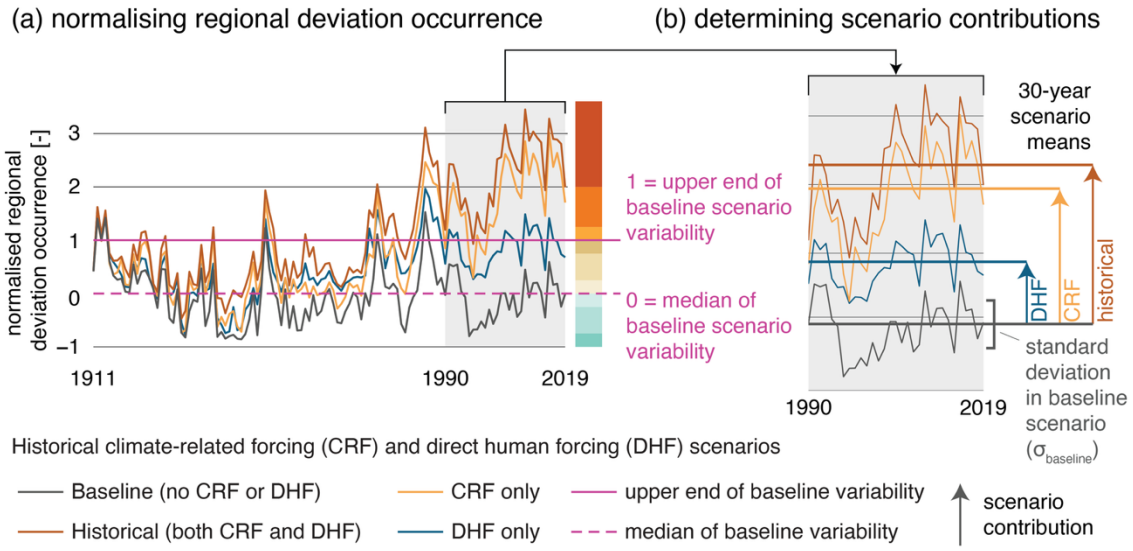

Figure 3. Normalising regional deviation occurrence and determining scenario contributions. To compare regions with different levels of natural variation in local deviations, regional occurrence of local deviations is first normalised with respect to the median and upper end of baseline scenario variability (a), before taking 30-year means for different climate-related forcing and direct human forcing scenarios and assessing their contributions to regional deviation occurrence (b). Annual ensemble medians are taken for all scenarios before normalisation. Steps a–b are described in detail in Methods.

The normalised regional occurrence of local deviations varies widely across dry and wet streamflow and soil moisture deviations and 1,268 regions represented in the analysis (Fig. 4). Regions with the highest occurrence of local deviations include, for example, central Africa for dry streamflow deviations (Fig. 4a), Maritime Southeast Asia for dry soil moisture deviations (Fig. 4c), and much of the northern

boreal zone for wet streamflow and soil moisture deviations (Fig. 4b, d). In regions including the Congo basin and eastern Australia, for instance, the normalised occurrence of wet deviations in both streamflow and soil moisture shows negative values, suggesting less frequent instances of wet local deviations (Fig. 4b, d). These regions have thus experienced an overall drying trend, in which not only dryness has increased but also wetness has decreased. Regions with values below but near to one, such as Central Europe and parts of western North America for dry streamflow and soil moisture deviations, have not yet crossed their region-specific upper end boundary but are close to doing so (Fig. 4a, c). Meanwhile, regions with values near zero – including e.g. Central Siberia for dry deviations (Fig. 4a, c) and parts of southern Africa for wet deviations (Fig. 4b, d) – are close to their respective baseline conditions. However, the occurrence of local deviations is affected by both CRF and DHF, which can either amplify or counter each other. Therefore, even regions with near-zero normalised deviation occurrence can be undergoing hydrological change.

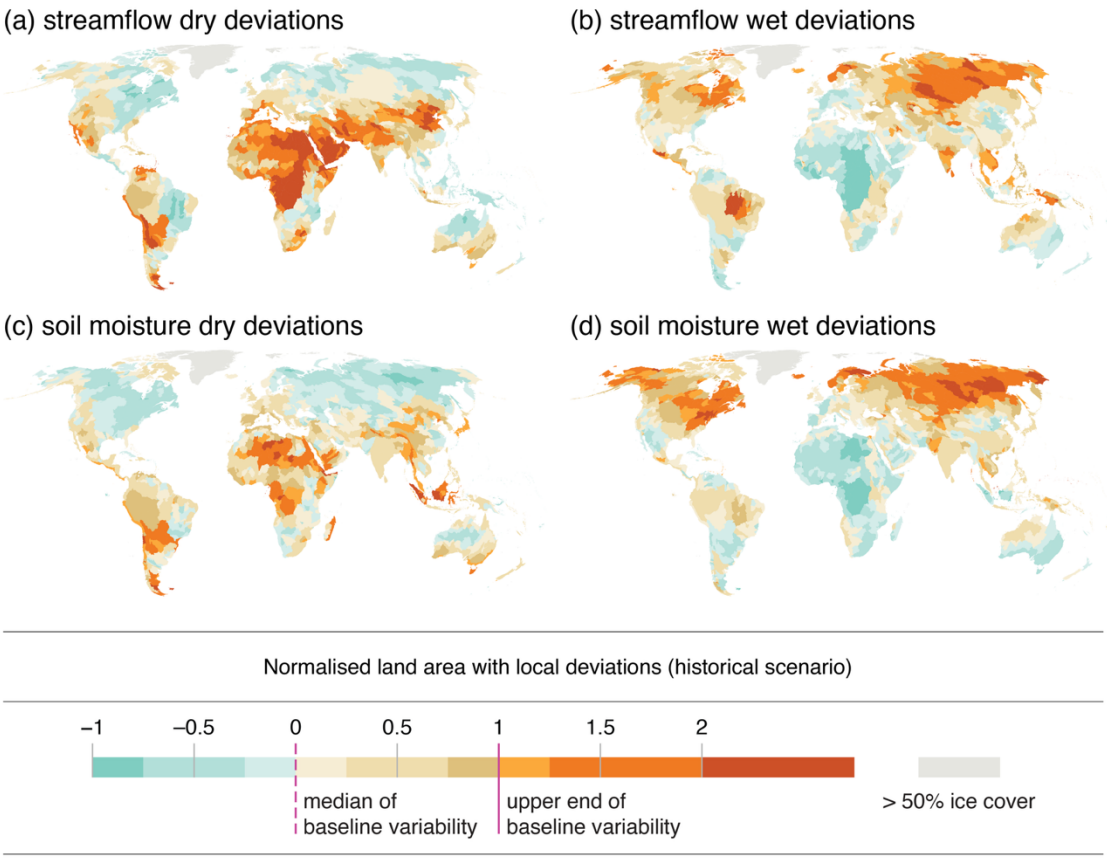

Figure 4. Regional occurrence of dry and wet local deviations for the historical scenario. The regional occurrence of local deviations is measured by the normalised percentage share of regional ice-free land area with local deviations, for dry streamflow deviations (a), wet streamflow deviations (b), dry soil moisture deviations (c), and wet soil moisture deviations (d). Shown is the 30-year mean (1990–2019) regional deviation occurrence, taken from annual ensemble medians (Fig. 3a, Methods). Regional dry and wet deviation occurrence for scenarios consisting of climate-related forcing only or direct human forcing only are shown in Supplementary Fig. 5–6.

Decomposition of regional CRF and DHF contributions

To assess historical CRF and DHF contributions on the regional occurrence of local deviations, we compared the average normalised occurrence of local deviations over the last 30 years of our study period (1990–2019) across all scenarios (Fig. 3b, Methods). We subtracted the 30-year mean of normalised regional deviation occurrence under the baseline scenario from the 30-year mean of the three other scenarios (historical, CRF only, DHF only) to quantify how each scenario alone affects regional deviation occurrence (Fig. 3b, Methods). Subsequently, we compared these differences to regionally typical interannual variability in local deviation occurrence, quantified by standard deviation in regional deviation occurrence under the baseline scenario during years 1990–2019 ($\sigma_{baseline}$; Fig. 3b, Methods). If CRF or DHF contributions exceeded $\sigma_{baseline}$, we marked their contribution "strong", whereas for contributions beyond $2\sigma_{baseline}$ were labelled as "very strong" (Fig. 5, Methods). This categorisation can thus distinguish how strongly CRF and DHF contribute to historical streamflow and soil moisture changes in each region.

Overall, the patterns of CRF and DHF contributions to regional deviation occurrence (Fig. 5) are in line with globally aggregated outcomes (Fig. 2). Strong CRF contributions are the most pronounced for wet deviations in the boreal zone (Fig. 5b, d) and for dry deviations in much of Africa (Fig. 5a, c). DHF contributes strongly to dry streamflow deviations in agriculturally intensive regions, such as India, Central Asia, and the western U.S. (Fig. 5a) and to dry soil moisture deviations in Southeast Asia (Fig. 5c). Wet deviations are primarily climate-driven, and only few locations in individual regions across North America, South and Central Asia, and the Nile basin show strong DHF influence on wet deviations (Fig. 5b, d).

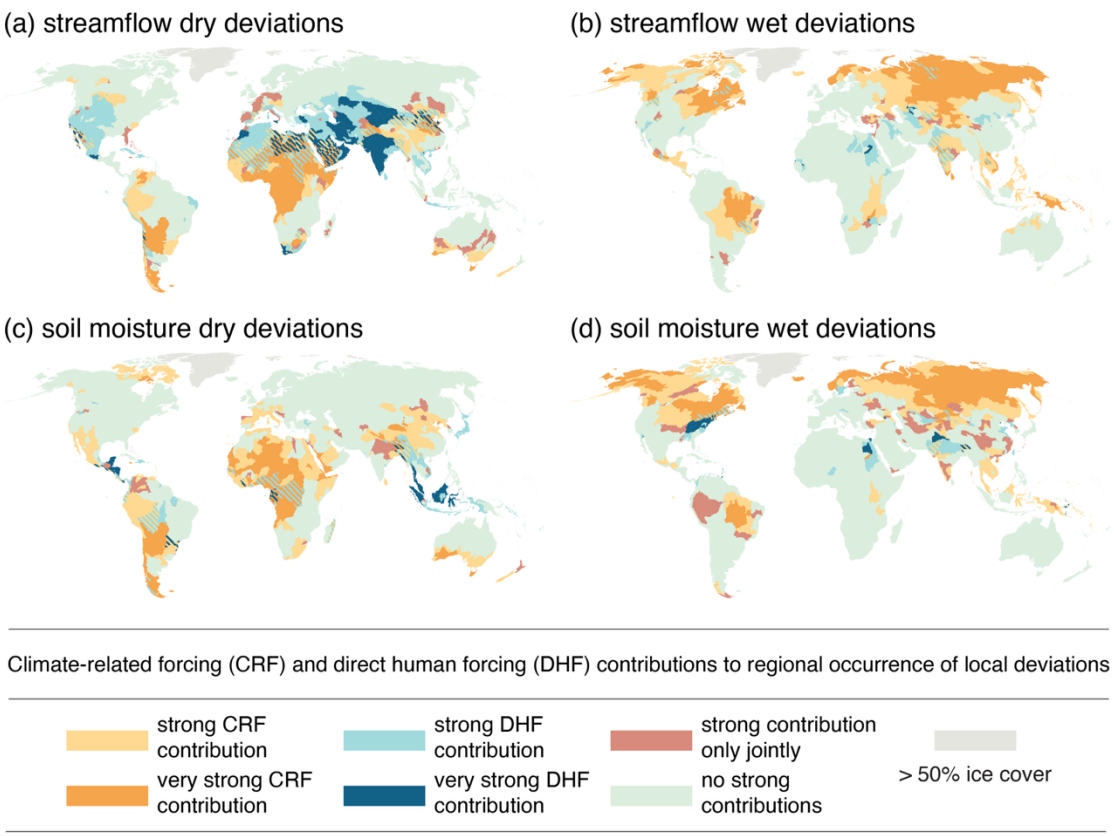

Figure 5. Contributions of climate-related forcing (CRF) and direct human forcing (DHF) to regional occurrence of local deviations. The CRF and DHF contributions are based on comparison between each scenario against the baseline scenario (Fig. 3b, Methods), for dry streamflow deviations (a), wet streamflow deviations (b), dry soil moisture deviations (c), and wet soil moisture deviations (d). Before assigning contributions, 30-year means (1990–2019) of regional deviation occurrence are taken from annual ensemble medians (Fig. 3a, Methods). Contributions are denoted as "strong" if a scenario contribution exceeds regionally typical interannual variability under the baseline scenario, measured by the standard deviation in regional deviation occurrence under the baseline scenario during 1990–2019, and "very strong" if the contribution is more than double the typical interannual variability (Methods). Hatched fill in a region denotes a combination of strong and/or very strong contribution from both CRF and DHF.

The spatial patterns of strong CRF and DHF contributions are, to a wide extent, polarised, because the overlap between regions experiencing strong or very strong influence from both CRF and DHF is relatively limited (Fig. 5). While all subcomponents show some individual regions with strong contributions from both CRF and DHF, only dry streamflow deviations have received strong contributions from both forcings across larger extents, such as northern China, the Arabian Peninsula and northern Africa (Fig. 5). For most regions with strong CRF or DHF contributions, both forcings contribute to net increase in the regional occurrence of deviations (Supplementary Fig. 7). However, exceptions can be found, for instance, in Central Asia and India where CRF decreases and DHF increases dry streamflow deviations (Supplementary Fig. 7a), and in the northernmost regions of the boreal zone where CRF increases and DHF decreases wet streamflow deviations (Supplementary Fig. 7b). This can suggest cases where human influence on streamflow (such as water use or reservoir

operation) is so substantial that it counters the background signal of climate change. Parts of southern China and southwestern North America exemplify areas in which regional occurrence of deviations does not yet exceed some of the region-specific upper end boundaries (Fig. 4), but CRF or DHF contributions are strong (Fig. 5). These cases highlight regions that may have undergone rapid change during the recent past decades.

Synthesis of regional CRF and DHF contributions

To synthesise how CRF and DHF affect regional deviation occurrence, we performed a global percentile ranking for CRF and DHF contributions in each of the four subcomponents of dry and wet deviations for both streamflow and soil moisture (Fig. 6; Methods). Higher percentile ranks for one subcomponent in a region indicate greater contribution of CRF or DHF to increasing deviation occurrence, compared to other regions. When taking the median percentile rank across the four subcomponents – each representing a different facet of the freshwater cycle – higher values signal greater deviation across many subcomponents and thus increased contribution of CRF or DHF on pervasive systemic freshwater changes (Fig. 6). In the CRF only scenario, these median percentile ranks show low variance across all regions globally (standard deviation = 0.11), with higher and lower median ranks distributed across all continents (Fig. 6a). This suggests widespread but comparatively uniform historical contributions of CRF on freshwater change. In contrast, the DHF only scenario has larger variance in median percentile ranks across all regions globally (standard deviation = 0.20) and shows more localised patterns. For instance, high median ranks locate to India and Central Asia, while lower median ranks are seen in the most northern latitudes and in many regions in Africa (Fig. 6b).

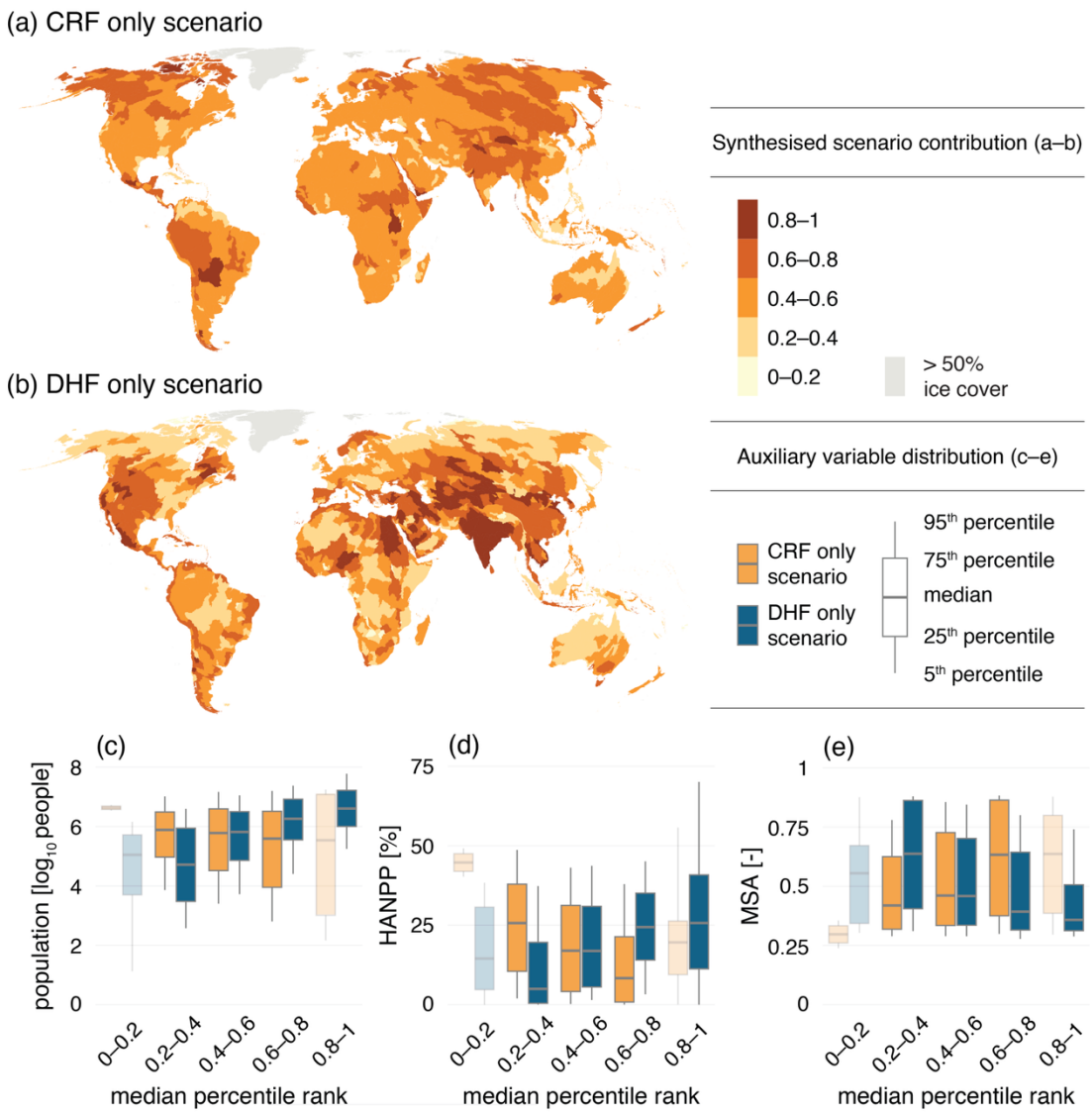

Figure 6. Synthesised contributions of climate-related forcing (CRF) and direct human forcing (DHF) on regional deviation occurrence together with a grouping of three auxiliary variables. Each region (n = 1,268) is assigned a global percentile rank based on CRF and DHF contribution values for each of the four subcomponents of regional deviation occurrence (streamflow and soil moisture, dry and wet) (Methods). Shown is the median of these four ranks in each region for the CRF only scenario (a) and the DHF only scenario (b). Median percentile ranks of panels a–b are further used to group three auxiliary variables (Methods): population count[36] (c), human appropriation of net primary production[37] (HANPP) (d), and mean species abundance[38] (MSA) (e). Regionally aggregated population count, HANPP, and MSA are shown in Supplementary Fig. 8, and group sizes for box plots in panels c–e are shown in Supplementary Table 1. Box plots with group sizes less than 5% of the total number of analysed regions are shaded in panels c–e, and box plot values outside of the 5th–95th percentile range are not shown.

Finally, to exemplify spatial correlations between regional freshwater deviations and human pressures on ecosystems, we used zonal statistics to summarise three auxiliary variables in median percentile rank bins shown in Fig. 6a–b (Methods). We summarised population count (Fig. 6c) and regional averages of human appropriation of net primary production (HANPP; Fig. 6d) and mean species abundance (MSA; Fig. 6e). Regions with the highest DHF contributions are associated with high population count

but no clear association between CRF contribution and population count can be found (Fig. 6c). HANPP and MSA – that both represent ecological impacts relative to undisturbed states – also show associations with the CRF and DHF contributions. High HANPP, which portrays increasing human disturbance of carbon and energy flows in ecosystems, appears positively associated with increasing DHF contributions and negatively associated with increasing CRF contributions (Fig. 6d). Low MSA, which depicts a high degree of ecosystem disturbance, is similarly associated with high DHF contributions (Fig. 6e). These associations suggest that the strongest CRF contributions are often located in regions where ecosystems are comparatively less altered (Supplementary Fig. 8b–c), but where climate change can still have a strong impact on streamflow and soil moisture (Fig. 6a). In contrast, the strongest DHF contributions (Fig. 6b) often co-occur spatially with human pressures on ecosystems (Supplementary Fig. 8b–c). Given that strong DHF likely indicates notable human dependencies – and impacts – on freshwater resources, the regions with strongest DHF contributions may be particularly vulnerable to further freshwater change and its adverse impacts.

Discussion

We demonstrate how the recently updated PB-FW can be extended towards an in-depth analysis of historical drivers of freshwater change across global and regional scales. Our findings highlight the continued increase in PB-FW transgression over the last 15 years (Fig. 1). Although the estimates' spread – including the previous[16] and the current, updated model ensemble – is large, our results align with research on recent trends in specific water cycle elements showing how the water cycle is undergoing widespread and regionally variable change[2,27–29]. Our results on the historical drivers of freshwater change (Fig. 5–6) largely agree with earlier conclusions of climatic factors affecting freshwater change across broad geographical scales[23,26], while direct human drivers can intensify this impact in specific regions where human dependencies on freshwater are also strong[5], especially in terms of increasingly dry conditions[22,24,39]. Projections of the water cycle[40–42] and our specific projections of the PB-FW suggest that in the future, returning back to pre-transgression conditions appears unlikely even with ambitious climate action, but the degree and rate of further change depend on the future climate change trajectory (Supplementary Text; Supplementary Fig. 9).

Interpreting the planetary boundaries framework in light of our findings emphasises the interconnectedness of Earth system processes represented by individual PBs[43,44]. Even in the hypothetical absence of direct human forcing, climate-related forcing alone would have transgressed the PB-FW notably (Fig. 2), which underscores how climate change – and thus the transgression of the climate change PB – is a major driver of PB-FW transgressions. The first PB-FW approaches that only considered human blue water consumption[19,21], as well as their further applications[25,45,46], neglect this systemic influence of climate and thus remain limited in their representation of freshwater-related risks in the Earth system. Therefore, in accordance with previous studies[1,31], we strongly advocate for

considering the freshwater cycle as a highly dynamic Earth system component instead of a controllable tap. Additionally, since our analysis shows alignment between freshwater change and other disturbances of the biosphere (Fig. 6), it serves as an early proof-of-concept application for simultaneously identifying regional drivers of freshwater change and vulnerabilities to its impacts. Investigating similar couplings in quantitative analyses of other PBs could aid in addressing critiques of the framework[47,48] and in broader goals of using the framework to inform sustainable environmental governance and Earth system stewardship[30,49,50].

Our approach has some key limitations that should be acknowledged. Numeric uncertainties stem largely from the simulated coarse scale data, although the models producing those data are as advanced as possible for a global-scale analysis (Methods) and first comprehensive validations of the ISIMIP 3a data are currently emerging[51,52]. Adopting the ensemble modelling approach can mitigate these uncertainties to an extent (Methods), but continued development and updates of the PB-FW analysis following the emergence of new models, data, and software[53] remains a recurring task. Moreover, separating increasingly precise human drivers, such as locally specific land and water management strategies, was not possible using the current ISIMIP data. Additionally – and perhaps most importantly – we here continue to presume that increasing frequencies of anomalous streamflow and soil moisture conditions are linked to an elevated level of freshwater-related Earth system risks[16,17]. Gathering systematic, empirically grounded evidence to evaluate this presumption and possibly adjusting local, regional and global boundaries based on that remains a top priority for improving the conceptualisation and quantification of cascading impacts and Earth system risks due to freshwater change.

Improved understanding of the interplay between climate-related and direct human forcing on driving freshwater change in regional contexts enhances the ability to assess, mitigate, or possibly adapt to its adverse impacts on the Earth system. However, our analysis is only a first step towards a more holistic approach, which should additionally connect the here-shown biophysical change with the higher-degree and system-specific telecoupled drivers of change[54]. For instance, regions with the highest historical changes in streamflow and soil moisture – that are often amplified by direct human forcing – may disproportionately contribute to freshwater-related Earth system risks. At the same time, high DHF contributions signal sustained dependence and impact on blue and green water resources. The external, non-biophysical drivers of that dependence (e.g. trade markets[55]) may, however, be located far from the biophysical change location, which complicates how human decisions ultimately affecting local and regional water resources are made[56,57]. Therefore, coupling these initial driving forces to the pathways ending in Earth system risks would be another vitally important next step. This could promote a transition from the PB framework's predominantly theoretical and biophysically oriented thinking to more holistic deliberation of the drivers and impacts of freshwater change in the Earth system.

Concluding remarks

Here, we show a reassessment and an extended analysis of the new planetary boundary for freshwater change (PB-FW). By leveraging an updated, maximally large ensemble of state-of-the-art global hydrological models, we extend the PB-FW assessment to 2019, together with an analysis of its historical drivers. The degree of PB-FW transgression has notably increased over the past 15 years, which has been driven predominantly by climate-related forcing (CRF). Direct human forcing (DHF), such as land cover change and water use, has particularly intensified dry deviations in regions with high human dependencies on blue and green water resources. Synthesising our multi-indicator analysis suggests how this freshwater change aligns with broader disturbance of the biosphere and how regions with strong DHF contributions may be particularly vulnerable to adverse impacts of freshwater change. Our approach thus allows for an increasingly systemic approach to assess hydrological change underlying the global PB-FW transgression. Intervening with this transgression, however, is only viable when coupling biophysical changes and impacts with their external, non-biophysical drivers, for which our approach takes a step forward. In summary, our work enhances the conceptual and practical utility of the PB-FW by offering an actionable use case for understanding freshwater change in the Earth system.

Methods

Climate-related forcing and direct human forcing scenarios

Our main data source was the Inter-Sectoral Impact Model Intercomparison Project (ISIMIP) data repository[34], from which we used data from the ISIMIP simulation round 3a experiments[33]. Hydrological data in the ISIMIP 3a experiments are simulated by global hydrological models (GHMs) using reanalysis-based climate-related forcing (CRF) and dynamic direct human forcing (DHF). CRF describes atmospheric variables, such as temperature and precipitation, which affect water availability and partitioning on the land surface. Some of the most important DHF variables include, for instance, land cover and use, cropping patterns, water abstraction, and flow regulation by dams and reservoirs, which further affect how water is distributed on the land surface and belowground.

To attribute the impact of CRF and DHF on hydrological change, we required four distinct simulation scenarios: 1) the baseline scenario with CRF derived from detrended historical climate reanalysis data and DHF at 1901 levels, 2) the historical scenario consisting of both historical CRF and DHF, 3) the CRF only scenario with DHF at 1901 levels, and 4) the DHF only scenario with CRF derived from detrended historical climate reanalysis data[33]. The CRF detrending procedure removes the global climate change trend from historical climate reanalysis data, but retains its internal variability, thus allowing the detrended climate data set to be used for climate change impact attribution[58]. While year 1901 levels do not mean a complete absence of DHF, the baseline scenario represents conditions that are largely absent from major anthropogenic modifications of the water cycle[33] and is thus adequately representative of pre-industrial-like reference conditions desired for the planetary boundaries framework[18].

GHMs participating in ISIMIP simulations are land surface models, which restricts the representation of hydrological impacts to the land surface (e.g. runoff propagation) and belowground (e.g. subsurface flows), leaving out land-atmosphere feedbacks (e.g. rainfall regulation by evapotranspiration) that would require coupling the GHM with an atmospheric model[59]. The GHMs participating in ISIMIP experiments, however, often have long legacies of extensive model development and validation[60–62], and the first validations of ISIMIP 3a hydrological data are continuously emerging[51,52], which is why we chose to leave an explicit validation outside of the scope of this study. Instead, we use the common and often adequate[63–65] ensemble modelling approach to mitigate uncertainties stemming from GHMs being subject to various process simplifications and variance in how they are implemented[66].

Model ensemble selection

In accordance with the previous analysis of the planetary boundary for freshwater change (PB-FW), we used streamflow as the control variable for blue water change and root-zone soil moisture (hereinafter

soil moisture) as the control variable for green water change[16]. Initially, we selected ISIMIP 3a simulation outputs from all GHMs for which outputs were available in all four required scenarios (baseline, historical, CRF only, DHF only). This yielded six GHMs available for streamflow (H08[67], HydroPy[68], JULES-W2[69], LPJmL5-7-10-fire[70], MIROC-INTEG-LAND[71], and WaterGAP2[61]) and four GHMs available for soil moisture (HydroPy, LPJmL5-7-10-fire, MIROC-INTEG-LAND, and WEB-DHM-SG[72]). Although available in the ISIMIP repository, we did not include JULES-W2-DDM30 for streamflow because the only difference to JULES-W2 is in the flow routing model implementation.

Simulations forced with three CRF data sets (GSWP3-W5E5, 20CRv3-ERA5, and 20CRv3-W5E5)[33,73] were available for models H08, WaterGAP2-2e, LPJmL5-7-10-fire and MIROC-INTEG-LAND, whereas simulations using only one CRF data set (GSWP3-W5E5) were available for HydroPy, JULES-W2 and WEB-DHM-SG. Additionally, although simulations using another CRF data set (20CRv3) were available, we did not select them because they ended in 2015, while data simulated with the other CRF data sets ended in 2019 or 2021[33]. Simulations with CRF from 20CRv3-ERA5 would have provided data until 2021, but to be consistent with 20CRv3-W5E5 and GSWP3-W5E5, we discarded the two last years from them.

Our analysis period thus consistently covered years 1901–2019 for all selected ensemble members (Supplementary Table 2). The spatial resolution of the gridded hydrological data was 0.5 degrees (approximately 50x50 km at the Equator). Streamflow data were delivered at monthly time resolution in units m^3/s, whereas soil moisture data were delivered with units kg/m^2. Streamflow data and most soil moisture data required no further pre-processing, but soil moisture data simulated by LPJmL5-7-10-fire were provided in five depth layers, which were summed to yield total soil moisture. For both variables and all ensemble members, sporadic instances of missing or negative monthly values were filled with the mean of all non-missing and non-negative values of the respective grid cell, month, and simulation scenario.

When performing our primary global analysis (Fig. 1) for each ensemble member separately, we found that for some ensemble members, the baseline and historical scenarios were mismatched in the beginning of the 20th century when historical CRF and DHF should be in near agreement with the baseline scenario (Supplementary Fig. 10–11). This was the case for streamflow simulations from H08 and MIROC-INTEG-LAND forced with GSWP3-W5E5 (Supplementary Fig. 10c, k) and for soil moisture simulations from all LPJmL5-7-10-fire ensemble members (Supplementary Fig. 11b–d) and from MIROC-INTEG-LAND forced with GSWP3-W5E5 (Supplementary Fig. 11g). These ensemble members were discarded from the presented main results, however, global results including also the discarded ensemble members are shown in Supplementary Fig. 12.

After determining the maximally large ensemble and filtering it by the above listed temporal constraints and consistency checks, the final resulting ensemble sizes were n = 12 for streamflow and n = 4 for soil

moisture. The final streamflow data ensemble consisted of simulations from six different GHMs forced with three CRF data sets with equal counts (4 ensemble members each), whereas the final soil moisture data ensemble consisted of simulations from three different GHMs forced with three CRF data sets with 1, 1, and 2 ensemble members each (Supplementary Table 2). Thus, the selected model ensembles were not substantially biased towards individual GHMs or CRF data sets and they can be thought to capture a decent amount of model and forcing variance to provide robust results.

The selected model ensembles differ from the previous PB-FW analysis[16], which expectedly causes divergence between their results. Most notably, the CRF data sets used for ISIMIP 3a simulations are based on historical climate reanalysis instead of modelled climate from general circulation models. This appears to affect especially the degree of large-scale wetting, which is visible when comparing between estimates based on two different versions of streamflow data, both run with WaterGAP2 (Supplementary Fig. 1). Some updates in direct human forcing (e.g. population data) have also been made for ISIMIP 3a compared to the previously used ISIMIP 2b[16], but, for instance, land use patterns are identical between the two experiment rounds[33]. While not all GHMs are present in both studies, even those that are (H08, LPJmL, WaterGAP) use newer versions in ISIMIP 3a experiments; for instance, WaterGAP2-2e used in ISIMIP 3a has an updated database of lakes and reservoirs compared to previous versions[61].

Occurrence of local deviations

In determining the occurrence of local deviations – i.e. representing aggregate human impacts on the freshwater cycle globally and regionally – we closely followed the methodological framework conceptualised by Wang-Erlandsson et al.[17] and scrutinised by Porkka et al.[16]. Conceptually, we assumed that increasing frequencies of anomalous streamflow and soil moisture conditions at the local scale expose local environments to rare or unforeseen conditions that they might not be adapted to, and increasing simultaneous occurrence of these anomalous conditions over larger areas contributes to elevated freshwater-related Earth system risks[16,17].

We first established local variability bounds for each grid cell, month, and ensemble member, separately for streamflow and soil moisture. The grid cell specific 5th and 95th percentile values under the baseline scenario were defined as the local bounds. To avoid potential traces of model simulation spinup affecting the local bounds (best exemplified in Supplementary Fig. 10a–c), we discarded years 1901–1910 from determining the local bounds and from all subsequent steps. Second, we detected grid cell scale local deviations, i.e. monthly events of streamflow or soil moisture values falling outside of the local bounds. Monthly values below the local 5th percentile bound were marked as dry local deviations and monthly values above the local 95th percentile bound were marked as wet local deviations. The local deviations were determined in a binary fashion (deviated or not deviated), without further specifying how far from the respective local bound each dry or wet local deviation fell.

We estimated the occurrence of local deviations by aggregating them within all global land areas and regionally within HydroBASINS level 4 hydrological catchments[35]. For each month and ensemble member, and separately for streamflow and soil moisture, we summed up physical land areas of grid cells that were marked as local deviations, yielding land area with dry local deviations (Fig. 2c, e) and land area with wet local deviations (Fig. 2d, f); these two land areas were further summed to yield land area with dry and wet local deviations (Fig. 1, Fig. 2a–b). The three sums of land area with local deviations were related to the total global or regional land area, yielding percentage shares. Given that the local variability bounds were limited by the 5th–95th percentile range, expectedly 5% of all values were marked as dry local deviations and 5% as wet local deviations for each grid cell, month, and ensemble member in the baseline scenario. Thus, also the expected global or regional percentage of land area with local deviations was approximately 5% for dry and wet deviations in the baseline scenario, respectively.

Antarctica and other grid cells covered by permanent land ice were excluded from the land area aggregations using the History Database of the Global Environment (HYDE) version 3.2.1 anthrome classification[74]. The regional aggregation of local deviations additionally considered region boundaries that cut across coarse 0.5-degree grid cells, considering only the grid cell fraction that lies within the region boundary[75]; thus, the regional land area with local deviations could never exceed the total regional land area.

Finally, we used the occurrence of local deviations in the baseline scenario to demarcate two reference boundaries; the median of baseline variability and the upper end of baseline variability, both of which were set at the global scale and for each region separately. Before setting the reference boundaries, however, we took annual means of monthly percentages of land area with local deviations for dry deviations, wet deviations, and for dry and wet deviations; all for each ensemble member separately. Annual means were followed by taking ensemble medians of the three percentage shares, resulting in three time series (n = 109, over years 1911–2019) that described annual percentages of land area with dry, wet, and dry and wet local deviations. For each of these time series, the median value was defined as the median of baseline variability, and the 95th percentile value was defined as the upper end of baseline variability. At the global scale, the upper end of baseline variability for dry and wet local deviations corresponds to the PB-FW[16].

To compare the three other scenarios (historical, CRF only, DHF only) against the baseline scenario, we repeated the detection of local deviations against local variability bounds set by the baseline scenario, followed by estimation of local deviation occurrence through aggregating local deviations both globally and regionally. Annual means were taken similarly from monthly percentage shares of land area with deviations, followed by taking ensemble medians. Local variability bounds and the median and the upper end of baseline variability were set only once globally and for each region, and all scenarios were thus compared against the same baseline. Growth rates for global deviation

occurrence were estimated by statistically significant (p = 0.05; two-sided test) Theil-Sen regression slopes[76] over years 1990–2019.

Regional normalisation of deviation occurrence

We estimated the regional occurrence of local deviations within HydroBASINS level 4 catchment boundaries[35], comprising 1,268 regions that overlapped with the selected hydrological data and had less than 50% permanent ice cover. Regions with more than 50% permanent ice cover were omitted from the regional analysis, although non-ice grid cells within them were considered when aggregating the global land area with local deviations (as outlined above). The mean area of the selected 1,268 regions was 104,000 km^2, while the median region area was 60,300 km^2.

To compare the occurrence of local deviations across differently sized regions with variable ambient CRF and DHF, we normalised the regional land area with local deviations using the median and upper end of baseline variability as normalisation limits (Fig. 3a). We defined the region-specific median baseline variability value as value zero, and the region-specific upper end of baseline variability value as value one, followed by normalising regional land areas with local deviations according to Eq. 1–3.

condition for $areaLocDev_{s,y}$	resulting $areaLocDev_{s,y,norm}$	
$if\ areaLocDev_{s,y} < Med_{bsl}$	$= \frac{areaLocDev_{s,y} - Med_{bsl}}{Med_{bsl}}$	(1)
$if\ Med_{bsl} \leq areaLocDev_{s,y} \leq UpEnd_{bsl}$	$= \frac{areaLocDev_{s,y} - Med_{bsl}}{UpEnd_{bsl} - Med_{bsl}}$	(2)
$if\ areaLocDev_{s,y} > UpEnd_{bsl}$	$= 1 + \frac{areaLocDev_{s,y} - UpEnd_{bsl}}{UpEnd_{bsl}}$	(3)

In Eq. 1–3, $areaLocDev_{s,y}$ refers to a regional percentage of land area with local deviations in scenario s for year y, Med_{bsl} to the region-specific median of baseline variability, $UpEnd_{bsl}$ to the region-specific upper end of baseline variability and $areaLocDev_{s,y,norm}$ to the normalised regional land area with local deviations in scenario s for year y.

Normalised regional deviation occurrence shows how close to the reference boundaries deviation occurrence in each scenario is in each region. Additionally, increasing local deviation occurrence in regions with high natural variance under the baseline scenario does not affect the normalised metric as much as the same amount of increasing absolute (percentage point) local deviation occurrence in regions with lower natural variance under the baseline scenario. To further account for interannual variability, we took 30-year means of the normalised regional land areas with local deviations over 1990–2019 before mapping them (Fig. 4, Supplementary Fig. 3–6).

Contributions of CRF and DHF scenarios

After normalising the regional occurrence of local deviations, we compared the historical, CRF only, and DHF only scenarios against the baseline scenario to determine how much each scenario contributes to the regional deviation occurrence (Fig. 3b). We first took the 30-year mean of normalised regional deviation occurrence in the baseline scenario over 1990–2019 (Eq. 4), followed by determining scenario contributions, i.e. differences between each scenario and the baseline scenario, using 30-year means of normalised regional deviation occurrence also for the other scenarios (Eq. 5). The standard deviation of normalised regional deviation occurrence under baseline conditions (taken similarly over 1990–2019 as the mean) (Eq. 6) was used as a benchmark value to further categorise the contribution strength of each scenario. Should a contribution diverge from the baseline with a value beyond that typical interannual variability under baseline conditions (Eq. 6), the contribution was marked "strong" (Eq. 7) or "very strong" (Eq. 8).

$$\mu_{bsl} = \frac{1}{30}\sum_{y=1}^{30} areaLocDev_{bsl,1990+(y-1),norm} \tag{4}$$

$$cntr_s = \frac{1}{30}\sum_{y=1}^{30} areaLocDev_{s,1990+(y-1),norm} - \mu_{bsl} \tag{5}$$

$$\sigma_{bsl} = \sqrt{\frac{1}{30}\sum_{y=1}^{30} (areaLocDev_{bsl,1990+(y-1),norm} - \mu_{bsl})^2} \tag{6}$$

condition for $cntr_s$	resulting $cntr_s$ label	
$if\ cntr_s > \sigma_{bsl}$	$cntr_s =$ "strong"	(7)
$if\ cntr_s > 2\sigma_{bsl}$	$cntr_s =$ "very strong"	(8)

In Eq. 4–8, $areaLocDev_{s,y,norm}$ is yielded from Eq. 1–3 and represents normalised regional land area with local deviations in scenario s for year y, and $cntr_s$ represents a contribution from scenario s.

The scenario contributions allowed us to compare the different strengths of CRF and DHF in increasing the regional occurrence of local deviations (Fig. 5). By Eq. 7–8, strong contributions were only defined towards increasing regional occurrence of deviations; strong contributions towards decreasing regional occurrence of deviations were not defined. However, scenario contributions (Eq. 5) could be negative,

547 which allowed us to evaluate whether both CRF and DHF increase regional deviation occurrence or if
548 one of them increases and one of them decreases regional deviation occurrence (Supplementary Fig. 7).

549 Synthesis of CRF and DHF contributions

550 We synthesised our analysis of CRF and DHF contributions on regional deviation occurrence across
551 four distinct subcomponents – dry and wet deviations for both streamflow and soil moisture (Fig. 6).
552 The synthesis consisted of assigning global percentile ranks for CRF and DHF contributions in each
553 subcomponent and taking the regional median of these ranks. Prior to percentile ranking, CRF and DHF
554 scenario contributions were related to the standard deviation of normalised regional deviation
555 occurrence under baseline conditions (Eq. 9) to account for region-specific natural variability.

$$cntr_{s,subComp,relative} = \frac{cntr_{s,subComp}}{\sigma_{bsl}} \quad (9)$$

556 In Eq. 9, σ_{bsl} is yielded from Eq. 6 and $cntr_{s,subComp}$ from Eq. 5 for CRF only and DHF only scenarios
557 and the four subcomponents of dry and wet deviations for both streamflow and soil moisture. Percentile
558 ranks were subsequently assigned for each $cntr_{s,subComp,relative}$ across all regions (n = 1,268).

559 Furthermore, we binned the CRF and DHF contribution percentile ranks to five bins and summarised
560 three auxiliary variables within them (Fig. 6c–e). The variables consisted of year 2019 population count
561 from the HYDE database version 3.4[36], year 2010 human appropriation of net primary production[37]
562 (HANPP), and year 2015 mean species abundance[38] (MSA). All variables were aggregated regionally
563 before summarising them. Prior to regional aggregation, population count and MSA required no pre-
564 processing. HANPP as a percentage of net primary production (NPP) was formed by summing the three
565 HANPP components (harvest, land use change, and deforestation) and relating the sum to potential NPP
566 to yield percentage shares, in accordance with the HANPP framework[37]. In regional aggregation,
567 population count was summed from grid cells overlapping with each region, whereas HANPP
568 (percentage) and MSA (unitless) were aggregated regionally using grid cell area weighted averages. All
569 operations considered only the grid cell fractions that were within the region boundaries[75] and weighted
570 the population sum or regional average accordingly.

Data availability

All data used in this study were gathered from openly available sources, which are appropriately cited in Methods. Output data produced by our analysis will be deposited in a public database upon publication of the article.

Code availability

The code used in collecting the data and producing the results shown will be made publicly available upon publication of the article.

References

1. Gleeson, T. *et al.* Illuminating water cycle modifications and Earth system resilience in the Anthropocene. *Water Resour. Res.* **56**, e2019WR024957 (2020).
2. Gudmundsson, L. *et al.* Globally observed trends in mean and extreme river flow attributed to climate change. *Science* **371**, 1159–1162 (2021).
3. McDermid, S. *et al.* Irrigation in the Earth system. *Nat. Rev. Earth Environ.* **4**, 435–453 (2023).
4. Smith, C., Baker, J. C. A. & Spracklen, D. V. Tropical deforestation causes large reductions in observed precipitation. *Nature* **615**, 270–275 (2023).
5. Zhao, G. *et al.* Decoupling of surface water storage from precipitation in global drylands due to anthropogenic activity. *Nat. Water* **3**, 80–88 (2025).
6. Dainese, M. *et al.* Global change experiments in mountain ecosystems: A systematic review. *Ecol. Monogr.* **94**, e1632 (2024).
7. Rohde, M. M. *et al.* Groundwater-dependent ecosystem map exposes global dryland protection needs. *Nature* **632**, 101–107 (2024).
8. Rolls, R. J. *et al.* Scaling biodiversity responses to hydrological regimes. *Biol. Rev.* **93**, 971–995 (2018).
9. Song, J. *et al.* Serious underestimation of reduced carbon uptake due to vegetation compound droughts. *Npj Clim. Atmospheric Sci.* **7**, 23 (2024).
10. Treat, C. C. *et al.* Permafrost Carbon: Progress on Understanding Stocks and Fluxes Across Northern Terrestrial Ecosystems. *J. Geophys. Res. Biogeosciences* **129**, e2023JG007638 (2024).
11. Staal, A. *et al.* Hysteresis of tropical forests in the 21st century. *Nat. Commun.* **11**, 4978 (2020).
12. Theeuwen, J. J. E., Staal, A., Tuinenburg, O. A., Hamelers, B. V. M. & Dekker, S. C. Local moisture recycling across the globe. *Hydrol. Earth Syst. Sci.* **27**, 1457–1476 (2023).
13. De Petrillo, E. *et al.* Reconciling tracked atmospheric water flows to close the global freshwater cycle. *Commun. Earth Environ.* **6**, 347 (2025).
14. Wang-Erlandsson, L. *et al.* Remote land use impacts on river flows through atmospheric teleconnections. *Hydrol. Earth Syst. Sci.* **22**, 4311–4328 (2018).
15. Messager, M. L., Dickens, C. W. S., Eriyagama, N. & Tharme, R. E. Limited comparability of global and local estimates of environmental flow requirements to sustain river ecosystems. *Environ. Res. Lett.* **19**, 024012 (2024).
16. Porkka, M. *et al.* Notable shifts beyond pre-industrial streamflow and soil moisture conditions transgress the planetary boundary for freshwater change. *Nat. Water* **2**, 262–273 (2024).
17. Wang-Erlandsson, L. *et al.* A planetary boundary for green water. *Nat. Rev. Earth Environ.* **3**, 380–392 (2022).
18. Richardson, K. *et al.* Earth beyond six of nine planetary boundaries. *Sci. Adv.* **9**, eadh2458 (2023).
19. Rockström, J. *et al.* Planetary Boundaries: Exploring the Safe Operating Space for Humanity. *Ecol. Soc.* **14**, (2009).
20. Gerten, D. *et al.* Towards a revised planetary boundary for consumptive freshwater use: role of environmental flow requirements. *Curr. Opin. Environ. Sustain.* **5**, 551–558 (2013).
21. Steffen, W. *et al.* Planetary boundaries: Guiding human development on a changing planet. *Science* **347**, 1259855 (2015).

22. Collignan, J., Polcher, J., Bastin, S. & Quintana-Segui, P. Identifying and Quantifying the Impact of Climatic and Non-Climatic Drivers on River Discharge in Europe. *Water Resour. Res.* **61**, e2024WR038220 (2025).
23. Li, Y.-X., Leng, P., Kasim, A. A. & Li, Z.-L. Spatiotemporal variability and dominant driving factors of satellite observed global soil moisture from 2001 to 2020. *J. Hydrol.* **654**, 132848 (2025).
24. Liu, Y., Yang, Y. & Song, J. Variations in Global Soil Moisture During the Past Decades: Climate or Human Causes? *Water Resour. Res.* **59**, e2023WR034915 (2023).
25. Pastor, A. V. *et al.* Understanding the transgression of global and regional freshwater planetary boundaries. *Philos. Trans. R. Soc. Math. Phys. Eng. Sci.* **380**, 20210294 (2022).
26. Virkki, V. *et al.* Archetypal flow regime change classes and their associations with anthropogenic drivers of global streamflow alterations. *Environ. Res. Commun.* **6**, 111007 (2024).
27. Gu, G. & Adler, R. F. Observed variability and trends in global precipitation during 1979–2020. *Clim. Dyn.* **61**, 131–150 (2023).
28. Lal, P., Shekhar, A., Gharun, M. & Das, N. N. Spatiotemporal evolution of global long-term patterns of soil moisture. *Sci. Total Environ.* **867**, 161470 (2023).
29. Rodell, M. *et al.* Emerging trends in global freshwater availability. *Nature* **557**, 651–659 (2018).
30. Downing, A. S. *et al.* Matching scope, purpose and uses of planetary boundaries science. *Environ. Res. Lett.* **14**, 073005 (2019).
31. Gleeson, T. *et al.* The Water Planetary Boundary: Interrogation and Revision. *One Earth* **2**, 223–234 (2020).
32. Han, S., Leng, G. & Yu, L. Review of Quantitative Applications of the Concept of the Water Planetary Boundary at Different Spatial Scales. *Water Resour. Res.* **59**, e2022WR033646 (2023).
33. Frieler, K. *et al.* Scenario setup and forcing data for impact model evaluation and impact attribution within the third round of the Inter-Sectoral Model Intercomparison Project (ISIMIP3a). *Geosci. Model Dev.* **17**, 1–51 (2024).
34. Gosling, S. N. *et al.* ISIMIP3a Simulation Data from the Global Water Sector. ISIMIP Repository https://doi.org/10.48364/ISIMIP.398165.5 (2025).
35. Lehner, B. & Grill, G. Global river hydrography and network routing: baseline data and new approaches to study the world's large river systems. *Hydrol. Process.* **27**, 2171–2186 (2013).
36. Klein Goldewijk, K. HYDE data for the Global Carbon Budget (2024). Utrecht University https://doi.org/10.24416/UU01-BV65K3 (2025).
37. Kastner, T. *et al.* Land use intensification increasingly drives the spatiotemporal patterns of the global human appropriation of net primary production in the last century. *Glob. Change Biol.* **28**, 307–322 (2022).
38. Schipper, A. M. *et al.* Projecting terrestrial biodiversity intactness with GLOBIO 4. *Glob. Change Biol.* **26**, 760–771 (2020).
39. Wada, Y., van Beek, L. P. H., Wanders, N. & Bierkens, M. F. P. Human water consumption intensifies hydrological drought worldwide. *Environ. Res. Lett.* **8**, 034036 (2013).
40. Bjarke, N., Livneh, B. & Barsugli, J. Storylines for Global Hydrologic Drought Within CMIP6. *Earths Future* **12**, e2023EF004117 (2024).
41. Lai, E. N., Wang-Erlandsson, L., Virkki, V., Porkka, M. & van der Ent, R. J. Root zone soil moisture in over 25% of global land permanently beyond pre-industrial variability as early as 2050 without climate policy. *Hydrol. Earth Syst. Sci.* **27**, 3999–4018 (2023).

42. Stevenson, S. *et al.* Twenty-first century hydroclimate: A continually changing baseline, with more frequent extremes. *Proc. Natl. Acad. Sci.* **119**, e2108124119 (2022).
43. Chrysafi, A. *et al.* Quantifying Earth system interactions for sustainable food production via expert elicitation. *Nat. Sustain.* **5**, 830–842 (2022).
44. Lade, S. J. *et al.* Human impacts on planetary boundaries amplified by Earth system interactions. *Nat. Sustain.* **3**, 119–128 (2020).
45. Hou, S. *et al.* Tracking grid-level freshwater boundary exceedance along global supply chains from consumption to impact. *Nat. Water* **3**, 439–448 (2025).
46. van Vuuren, D. P. *et al.* Exploring pathways for world development within planetary boundaries. *Nature* **641**, 910–916 (2025).
47. Biermann, F. & Kim, R. E. The Boundaries of the Planetary Boundary Framework: A Critical Appraisal of Approaches to Define a "Safe Operating Space" for Humanity. *Annu. Rev. Environ. Resour.* **45**, 497–521 (2020).
48. Ferretto, A., Matthews, R., Brooker, R. & Smith, P. Planetary Boundaries and the Doughnut frameworks: A review of their local operability. *Anthropocene* **39**, 100347 (2022).
49. Häyhä, T., Lucas, P. L., van Vuuren, D. P., Cornell, S. E. & Hoff, H. From Planetary Boundaries to national fair shares of the global safe operating space — How can the scales be bridged? *Glob. Environ. Change* **40**, 60–72 (2016).
50. Kim, R. E. & Kotzé, L. J. Planetary boundaries at the intersection of Earth system law, science and governance: A state-of-the-art review. *Rev. Eur. Comp. Int. Environ. Law* **30**, 3–15 (2021).
51. Heinicke, S. *et al.* Global hydrological models continue to overestimate river discharge. *Environ. Res. Lett.* **19**, 074005 (2024).
52. Otta, K., Müller Schmied, H., Gosling, S. N. & Hanasaki, N. Towards the use of satellite remote sensing to validate reservoir storage in global hydrological models: methodology and pilot study in the CONUS. *Environ. Res. Water* **1**, 015002 (2025).
53. Gerten, D. *et al.* A software package for assessing terrestrial planetary boundaries. *One Earth* **8**, (2025).
54. Liu, J. *et al.* Framing Sustainability in a Telecoupled World. *Ecol. Soc.* **18**, (2013).
55. Mekonnen, M. M. *et al.* Trends and environmental impacts of virtual water trade. *Nat. Rev. Earth Environ.* **5**, 890–905 (2024).
56. Moore, M.-L. *et al.* Moving from fit to fitness for governing water in the Anthropocene. *Nat. Water* **2**, 511–520 (2024).
57. Newig, J., Challies, E., Cotta, B., Lenschow, A. & Schilling-Vacaflor, A. Governing global telecoupling toward environmental sustainability. *Ecol. Soc.* **25**, (2020).
58. Mengel, M., Treu, S., Lange, S. & Frieler, K. ATTRICI v1.1 – counterfactual climate for impact attribution. *Geosci. Model Dev.* **14**, 5269–5284 (2021).
59. Drüke, M. *et al.* CM2Mc-LPJmL v1.0: biophysical coupling of a process-based dynamic vegetation model with managed land to a general circulation model. *Geosci. Model Dev.* **14**, 4117–4141 (2021).
60. Boulange, J., Yoshida, T., Nishina, K., Okada, M. & Hanasaki, N. Delivering the latest global water resource simulation results to the public. *Clim. Serv.* **30**, 100386 (2023).
61. Müller Schmied, H. *et al.* The global water resources and use model WaterGAP v2.2e: description and evaluation of modifications and new features. *Geosci. Model Dev.* **17**, 8817–8852 (2024).

62. Schaphoff, S. *et al.* LPJmL4 – a dynamic global vegetation model with managed land – Part 2: Model evaluation. *Geosci. Model Dev.* **11**, 1377–1403 (2018).
63. Huang, S. *et al.* Evaluation of an ensemble of regional hydrological models in 12 large-scale river basins worldwide. *Clim. Change* **141**, 381–397 (2017).
64. Kumar, A. *et al.* Multi-model evaluation of catchment- and global-scale hydrological model simulations of drought characteristics across eight large river catchments. *Adv. Water Resour.* **165**, 104212 (2022).
65. Zaherpour, J. *et al.* Exploring the value of machine learning for weighted multi-model combination of an ensemble of global hydrological models. *Environ. Model. Softw.* **114**, 112–128 (2019).
66. Müller Schmied, H. *et al.* Graphical representation of global water models. *Geosci. Model Dev.* **18**, 2409–2425 (2025).
67. Hanasaki, N., Yoshikawa, S., Pokhrel, Y. & Kanae, S. A global hydrological simulation to specify the sources of water used by humans. *Hydrol. Earth Syst. Sci.* **22**, 789–817 (2018).
68. Stacke, T. & Hagemann, S. HydroPy (v1.0): a new global hydrology model written in Python. *Geosci. Model Dev.* **14**, 7795–7816 (2021).
69. Best, M. J. *et al.* The Joint UK Land Environment Simulator (JULES), model description – Part 1: Energy and water fluxes. *Geosci. Model Dev.* **4**, 677–699 (2011).
70. Wirth, S. B. *et al.* Biological nitrogen fixation of natural and agricultural vegetation simulated with LPJmL 5.7.9. *Geosci. Model Dev.* **17**, 7889–7914 (2024).
71. Yokohata, T. *et al.* MIROC-INTEG-LAND version 1: a global biogeochemical land surface model with human water management, crop growth, and land-use change. *Geosci. Model Dev.* **13**, 4713–4747 (2020).
72. Qi, W. *et al.* Economic growth dominates rising potential flood risk in the Yangtze River and benefits of raising dikes from 1991 to 2015. *Environ. Res. Lett.* **17**, 034046 (2022).
73. Lange, S. Trend-preserving bias adjustment and statistical downscaling with ISIMIP3BASD (v1.0). *Geosci. Model Dev.* **12**, 3055–3070 (2019).
74. Klein Goldewijk, K., Beusen, A., Doelman, J. & Stehfest, E. Anthropogenic land use estimates for the Holocene – HYDE 3.2. *Earth Syst. Sci. Data* **9**, 927–953 (2017).
75. Baston, D. exactextractr: Fast Extraction from Raster Datasets using Polygons. (2023).
76. Hurtado, S. I. RobustLinearReg: Robust Linear Regressions. (2020).

Acknowledgements

We thank the ISIMIP modelling groups, the ISIMIP sector coordinators, and the ISIMIP cross-sectoral science team for making the hydrological model outputs available.

V.V. and M.P. acknowledge funding from the Strategic Research Council (SRC) established within the Research Council of Finland (grant no. 365752, 365754) and European Research Council (ERC) grant AQUAGUARD (grant no. 101118083). L.S.A. is part of PIK's Planetary Boundaries Science Lab. The funders had no role in the study design, data collection, analysis and conclusions presented here.

Funded by the European Union. Views and opinions expressed are however those of the author(s) only and do not necessarily reflect those of the European Union or the European Research Council Executive Agency. Neither the European Union nor the granting authority can be held responsible for them.

Author contributions

V.V., M.P., L.S.A., and S.t.W. conceptualised the study. V.V. gathered the data, designed the analyses, and derived the results shown in the paper, with help from all authors. V.V. led the writing of the manuscript with contributions from all authors.

Competing interests

The authors declare no competing interests.

Supplementary information for

Regionally divergent drivers behind transgressions of the freshwater change planetary boundary

This supplementary information includes:

Supplementary Text

Projecting global freshwater deviation occurrence to the future. Given the increasing contribution of climate-related forcing (CRF) in determining the status of the planetary boundary for freshwater change (PB-FW) (Fig. 2), we assessed projected future trajectories of global streamflow and soil moisture deviation occurrence under three climate change scenarios. The Inter-Sectoral Impact Model Intercomparison Project (ISIMIP) simulation round 3a data covers historical simulations ending in the year 2019[1] (Methods), which is why for the future projections, we switched to data from ISIMIP simulation round 3b experiments spanning years 1850–2100 in total[2,3]. Differing from ISIMIP 3a, which uses CRF based on historical reanalysis, data simulated by ISIMIP 3b experiments use CRF from climate reconstructions and projections derived from general circulation models (GCMs)[3].

We re-established the counterfactual baseline scenario using ISIMIP 3b data to avoid comparing hydrological simulations that would have different CRFs from reanalysis and GCMs. In the ISIMIP 3b baseline scenario, CRF is fixed at levels representing pre-industrial climate conditions (CO_2 and CH_4 concentrations at year 1850 levels), and direct human forcings (DHF) are equally fixed at year 1850 levels[3]. In historical simulations for years 1850–2014, both CRF and DHF follow historical changes[3]. For projecting future climate change impacts on global freshwater deviation occurrence for years 2015–2100, we used three scenarios comprising SSP1–RCP2.6 with low CO_2 emissions, SSP3–RCP7.0 with medium-to-high CO_2 emissions, and SSP5–RCP8.5 with high CO_2 emissions[3]. All future scenarios used fixed DHF at year 2015 levels, which means that possible DHF adaptation measures were not considered in the analysis, and the results display only the projected impact of future climate change.

We selected ISIMIP 3b simulation outputs from all global hydrological models (GHMs) for which outputs were available in all five required scenarios (baseline, historical, SSP1–RCP2.6, SSP3–RCP7.0, SSP5–RCP8.5). This yielded three GHMs available for streamflow (H08[4], MIROC-INTEG-LAND[5], and WaterGAP2[6]) and one GHM available for soil moisture (MIROC-INTEG-LAND). For all models, simulations forced with five GCM-based CRF data sets were available (from GFDL-ESM4, IPSL-CM6A-LR, MPI-ESM1-2-HR, MRI-ESM-2-0, and UKESM1-0-LL)[3,7]. The resulting ensemble sizes for future projections were thus n = 15 for streamflow and n = 5 for soil moisture.

Besides using ISIMIP 3b data, we otherwise performed the projections of global freshwater deviation occurrence similarly as for ISIMIP 3a data (Methods). We established local variability bounds (between 5^{th}–95^{th} percentile values) for each grid cell, month, and ensemble member, separately for streamflow and soil moisture, using years 1860–2014 from the baseline scenario. We then detected local deviations and aggregated them globally to yield monthly percentage shares of ice-free land area with local deviations. Annual means were taken from the monthly percentage shares, followed by taking ensemble medians. Ensemble median annual time series of land area with local deviations under the baseline scenario were finally used to set the median and upper end of baseline variability, using years 1860–

2014, and thus making the reference boundaries specific to the ISIMIP 3b counterfactual baseline scenario. This allowed for side-by-side comparison between historical and future projected global deviation occurrence. By the re-establishment of the baseline scenario and different hydrological model ensemble, however, the historical values were not directly comparable to those derived from ISIMIP 3a data.

Persistently continued deviations in the freshwater cycle. Projecting the global streamflow and soil moisture deviation occurrence to year 2100 shows mostly an increasing PB-FW transgression trajectory (Supplementary Fig. 9). While the higher-emission scenarios SSP3–RCP7.0 and SSP5–RCP8.5 point towards a persistent increase in global deviation occurrence across all subcomponents of the PB-FW, the low-emission SSP1–RCP2.6 scenario is projected to stabilise (Supplementary Fig. 9a, c–e) or begin declining (Supplementary Fig. 9b, f) the occurrence of local deviations. In 2100, streamflow deviations are projected to cover 26.1% (~33.9 million km^2) of ice-free land area in the SSP1–RCP2.6 scenario and 42.6% (~55.4 million km^2) in the SSP5–RCP8.5 scenario, whereas these figures are 28.2% (~36.7 million km^2) in the SSP1–RCP2.6 scenario and 40.2% (~52.3 million km^2) in the SSP5–RCP8.5 scenario for soil moisture, respectively. Despite the large scenario spread, the distinct shapes of the trajectories demonstrate the stabilising effect of the SSP1–RCP2.6 low-emission pathway, whereas higher-emission scenarios point towards continuously increasing PB-FW transgressions (Supplementary Fig. 9).

When comparing global freshwater deviation occurrence based on ISIMIP 3a simulations (reanalysis-based CRF; Fig. 2) and ISIMIP 3b simulations (GCM-based CRF; Supplementary Fig. 9), historical dry streamflow and soil moisture deviation occurrences are in relatively fair agreement, with year 2015 values around 13–15% (Fig. 3c, e; Supplementary Fig. 9c, e). However, 20th century wet deviation occurrence trajectories, especially for streamflow, are more divergent between results yielded from ISIMIP 3a and 3b simulations (Fig. 3d, f; Supplementary Fig. 9d, f), with ISIMIP 3b using GCM-based CRF showing less wet deviation occurrence. This could link to the divergent large-scale wetting signals between reanalysis-based and GCM-based CRFs, which is also seen in comparison of global streamflow deviation occurrence between ISIMIP 3a simulations and another set of global deviation occurrence estimates based on GCM-forced ISIMIP simulation round 2b experiments[8] (Supplementary Fig. 1). It should, additionally, be noted that while the baseline scenario appears trendless when using ISIMIP 3b data, traces of model spinup and discontinuities between historical and future scenarios are clearly visible around the year 2015 breakpoint between scenarios (Supplementary Fig. 9), which likely has a distorting effect on precise numerical estimates.

While the freshwater cycle has already been persistently altered and future climate change projections show how returning to conditions preceding PB-FW transgression appears unlikely, the degree and rate of further change remain dependent on climate change pathways. Notwithstanding large uncertainties and mismatches between simulations in the ISIMIP 3b ensemble, the ambition level of climate action

82 can possibly stabilise the PB-FW transgression trajectory – or continuously increase it, should CO_2
83 emissions remain at a high level. In future studies, increasing model ensemble sizes with the ongoing
84 yet incomplete ISIMIP 3b experiment round[3], correcting apparent mismatches at the breakpoint
85 between historical and future scenarios, adding DHF adaptation scenarios, and extending the analysis
86 to cover regionally explicit aspects would be warranted for a more elaborate outlook on future PB-FW
87 projections.

Supplementary Figures

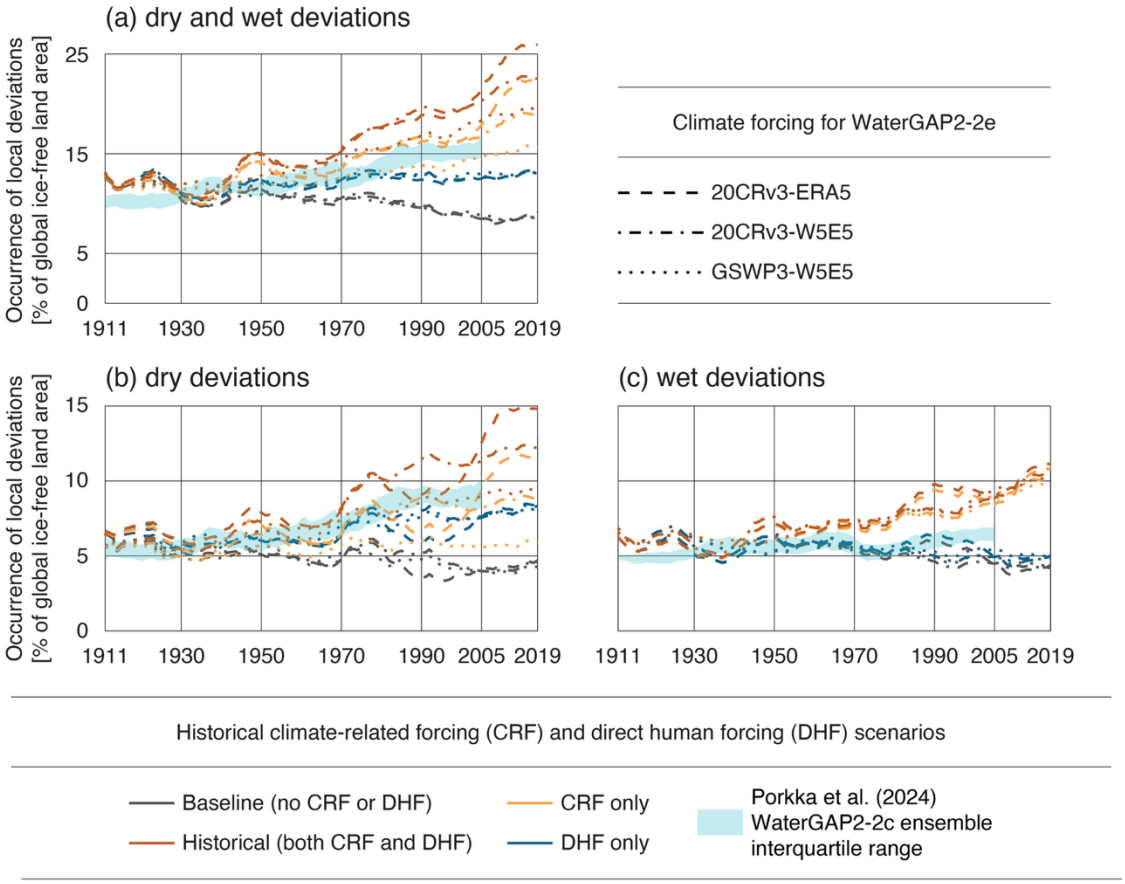

Supplementary Figure 1. Global occurrence of dry and wet local streamflow deviations under different climate-related forcing (CRF) and direct human forcing scenarios, separately for three WaterGAP2-2e simulations using three different CRF data sets. The global occurrence of local streamflow deviations is measured by the percentage share of global ice-free land area with local deviations, for dry and wet deviations (a), dry deviations (b), and wet deviations (c). Shown is the annual percentage, which is computed as an average of monthly percentages (Methods). Time series of the occurrence of local deviations and limits of the ensemble interquartile range (IQR) are smoothed with a 10-year moving (trailing) mean over the annual percentage and ensemble IQR limits, respectively. Benchmark values until year 2005 are taken from the previous PB-FW estimate, specifically for WaterGAP2-2c forced with CRF from four general circulation models[8].

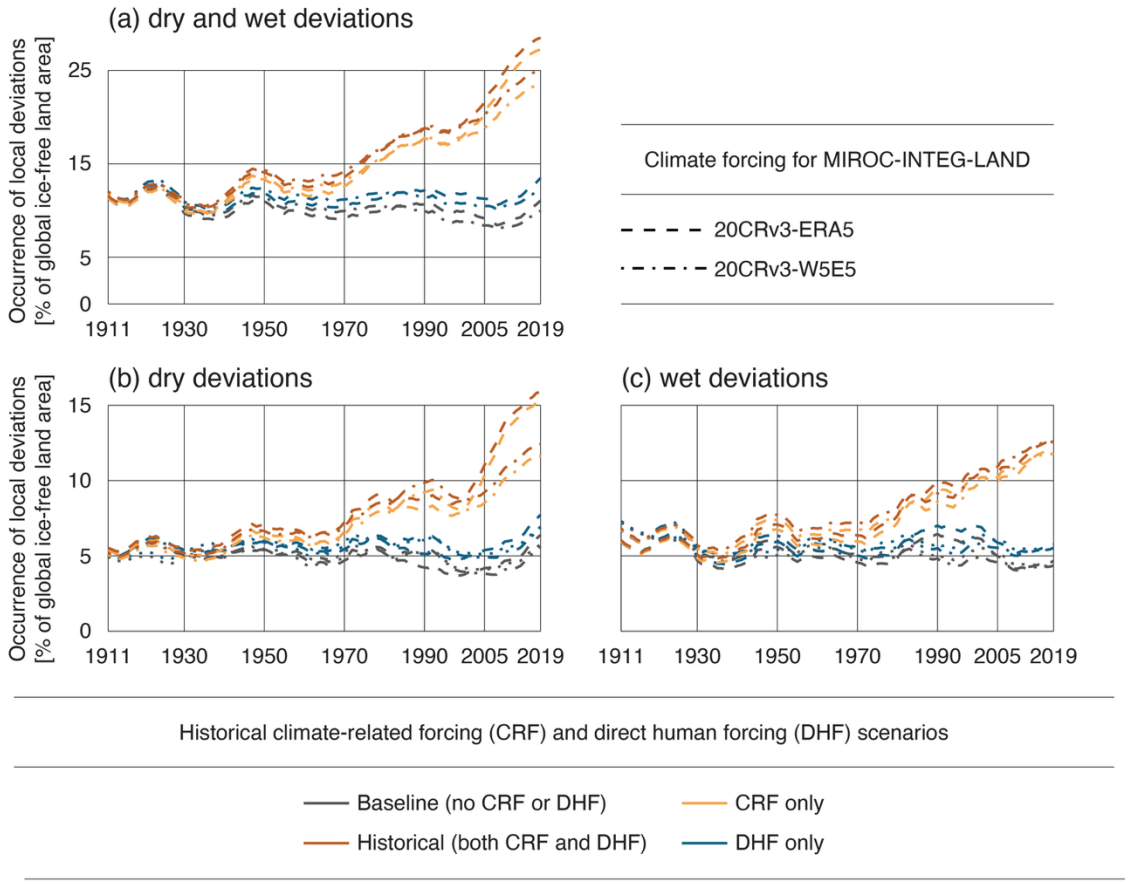

Supplementary Figure 2. Global occurrence of dry and wet local soil moisture deviations under different climate-related forcing and direct human forcing scenarios, separately for two MIROC-INTEG-LAND simulations using two different CRF data sets. The global occurrence of local soil moisture deviations is measured by the percentage share of global ice-free land area with local deviations, for dry and wet deviations (a), dry deviations (b), and wet deviations (c). Shown is the annual percentage, which is computed as an average of monthly percentages (Methods). Time series of the occurrence of local deviations are smoothed with a 10-year moving (trailing) mean over the annual percentage.

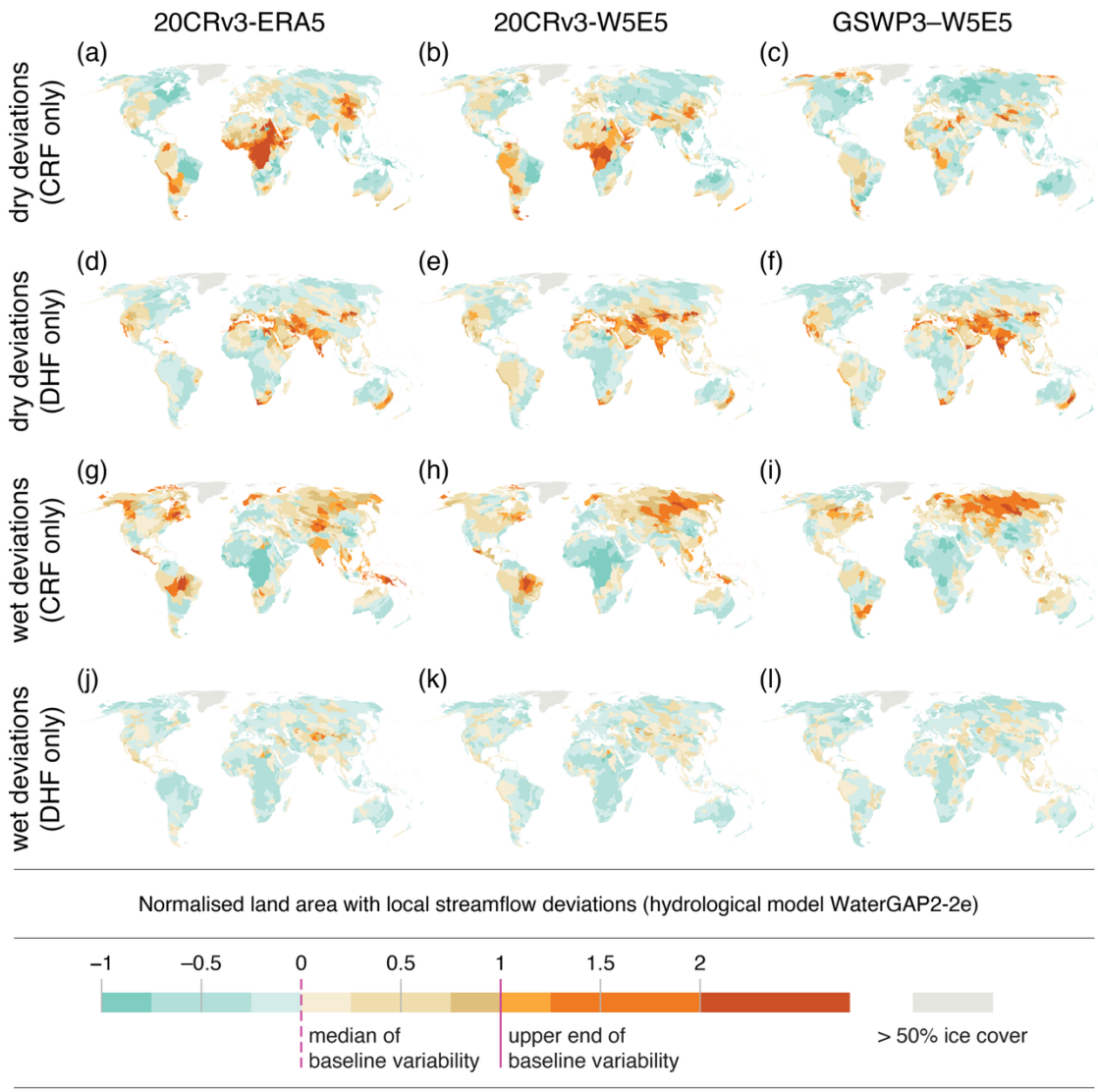

Supplementary Figure 3. Regional occurrence of dry and wet local streamflow deviations under different climate-related forcing (CRF) and direct human forcing scenarios, separately for three WaterGAP2-2e simulations using three different CRF data sets. The regional occurrence of local deviations is measured by the normalised percentage share of regional ice-free land area with local streamflow deviations, for dry deviations (a–f) and wet deviations (g–l). Shown is the 30-year mean (1990–2019) regional deviation occurrence, taken from annual averages (Fig. 3a, Methods).

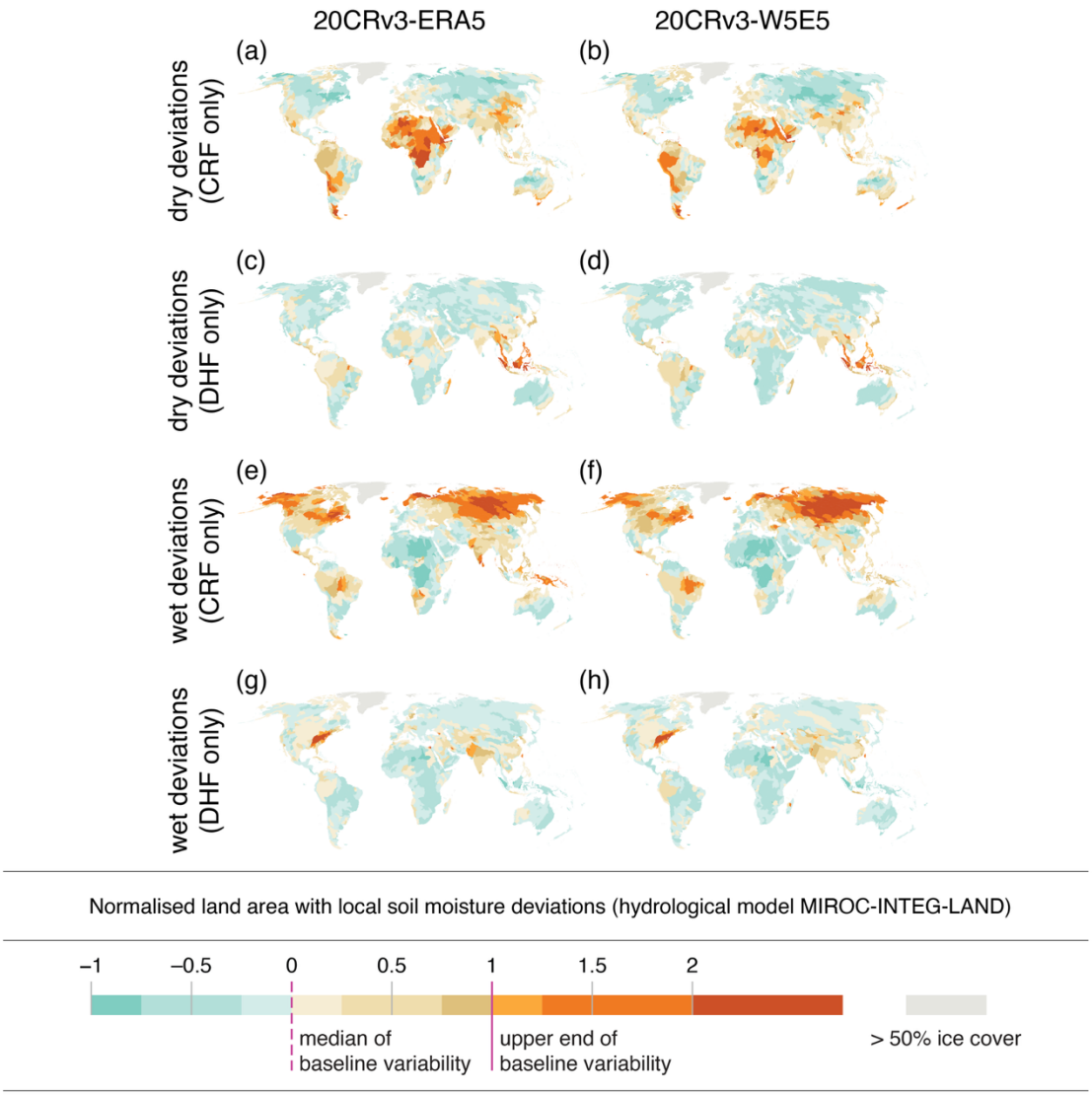

Supplementary Figure 4. Regional occurrence of dry and wet local soil moisture deviations under different climate-related forcing (CRF) and direct human forcing scenarios, separately for two MIROC-INTEG-LAND simulations using two different CRF data sets. The regional occurrence of local deviations is measured by the normalised percentage share of regional ice-free land area with local soil moisture deviations, for dry deviations (a–d) and wet deviations (e–h). Shown is the 30-year mean (1990–2019) regional deviation occurrence, taken from annual averages (Fig. 3a, Methods).

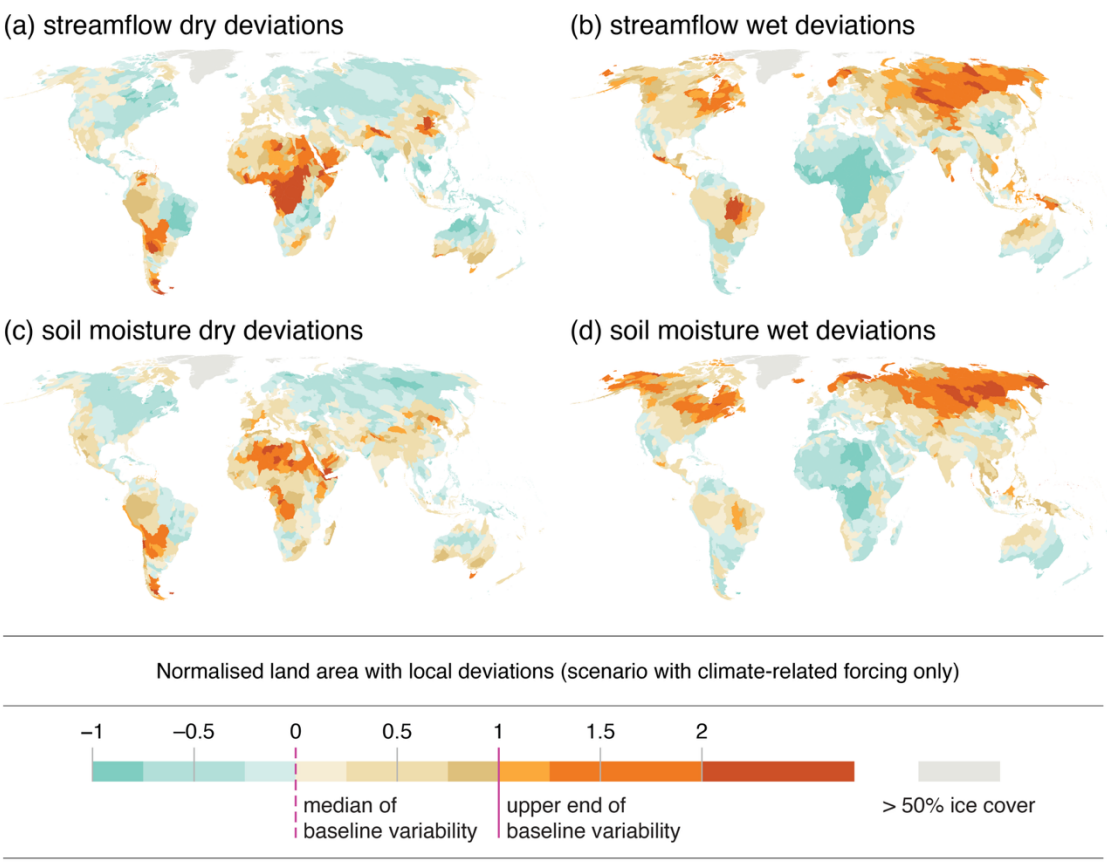

Supplementary Figure 5. Regional occurrence of dry and wet local deviations for a simulation scenario consisting of climate-related forcing only. The regional occurrence of local deviations is measured by the normalised percentage share of regional ice-free land area with local deviations, for dry streamflow deviations (a), wet streamflow deviations (b), dry soil moisture deviations (c), and wet soil moisture deviations (d). Shown is the 30-year mean (1990–2019) regional deviation occurrence, taken from annual ensemble medians (Fig. 3a, Methods).

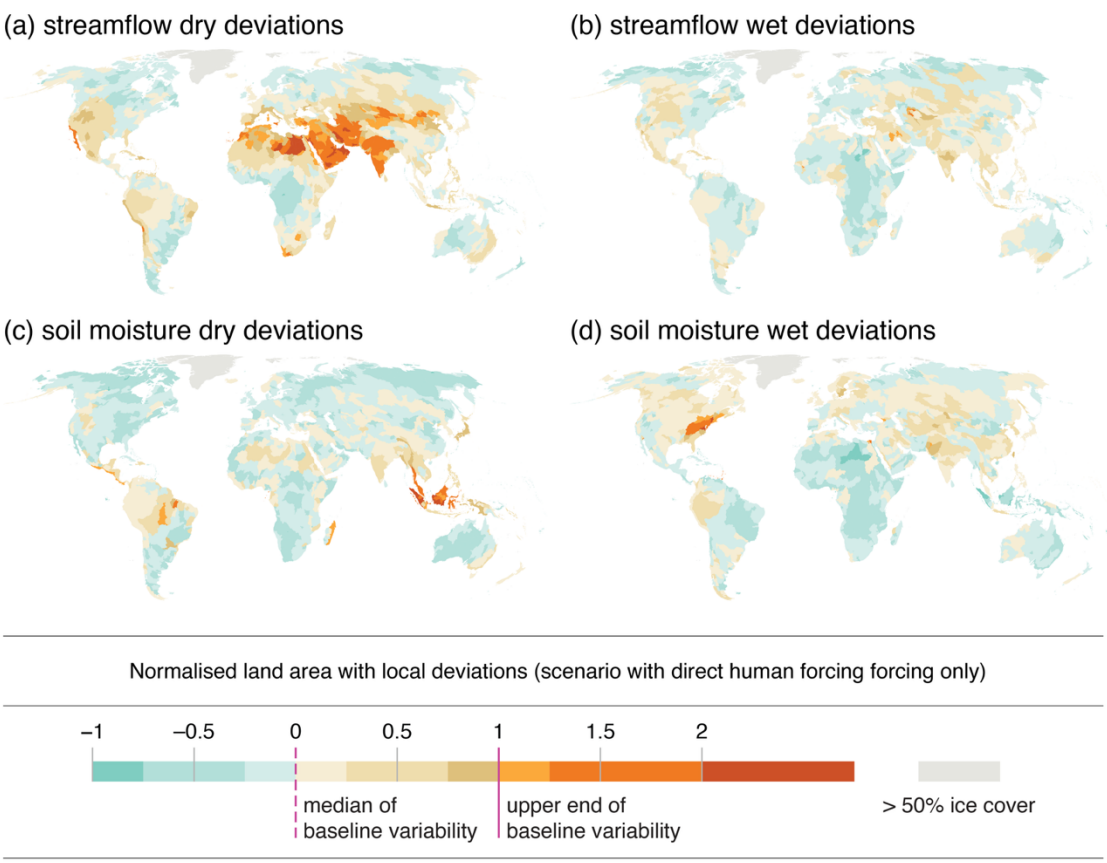

Supplementary Figure 6. Regional occurrence of dry and wet local deviations for a simulation scenario consisting of direct human forcing only. The regional occurrence of local deviations is measured by the normalised percentage share of regional ice-free land area with local deviations, for dry streamflow deviations (a), wet streamflow deviations (b), dry soil moisture deviations (c), and wet soil moisture deviations (d). Shown is the 30-year mean (1990–2019) regional deviation occurrence, taken from annual ensemble medians (Fig. 3a, Methods).

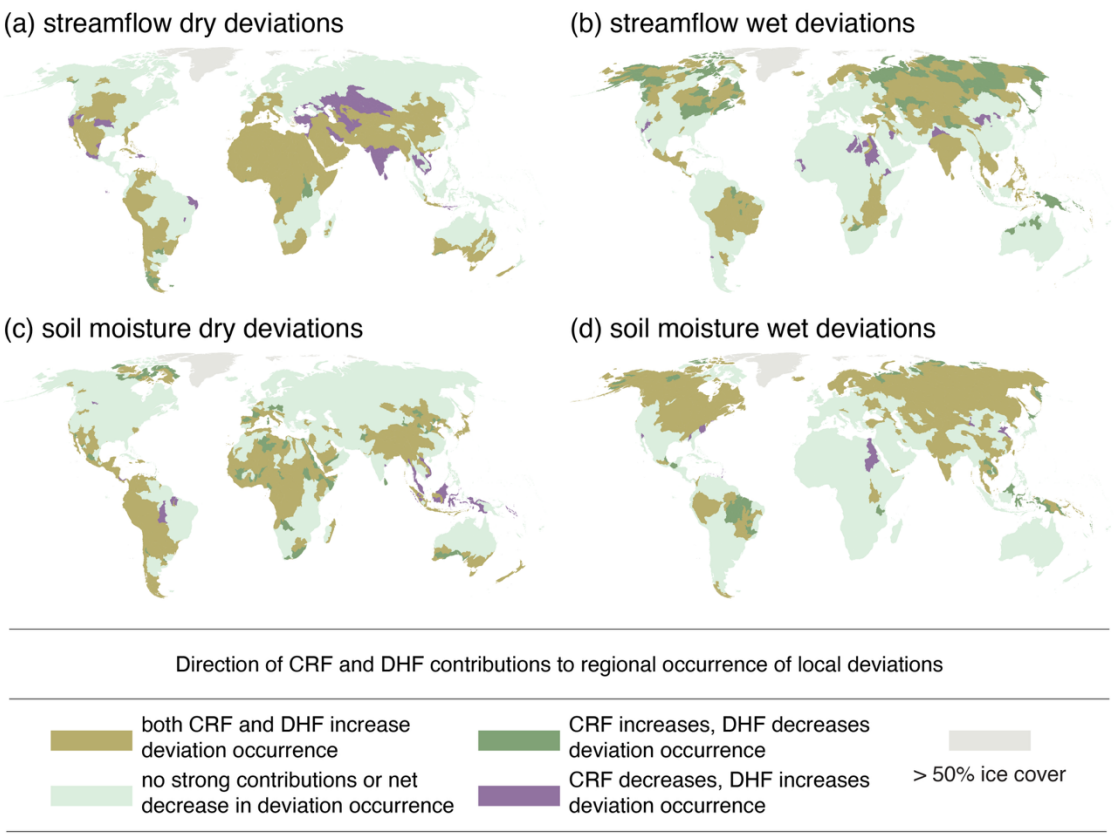

Supplementary Figure 7. Direction of climate-related forcing (CRF) and direct human forcing (DHF) contributions to increasing regional occurrence of local deviations. The CRF and DHF contributions are based on comparison between each scenario against the baseline scenario (Fig. 3b, Methods), for dry streamflow deviations (a), wet streamflow deviations (b), dry soil moisture deviations (c), and wet soil moisture deviations (d). Before assigning contributions, 30-year means (1990–2019) of regional deviation occurrence are taken from annual ensemble medians (Fig. 3a, Methods). The directions of CRF and DHF contributions are assigned for those regions in which one of the three contributions (CRF independently, DHF independently, CRF and DHF jointly) is strong or very strong (Fig. 5). If none of these contributions are strong or if net deviation occurrence decreases, the directions of CRF and DHF contributions are not assigned.

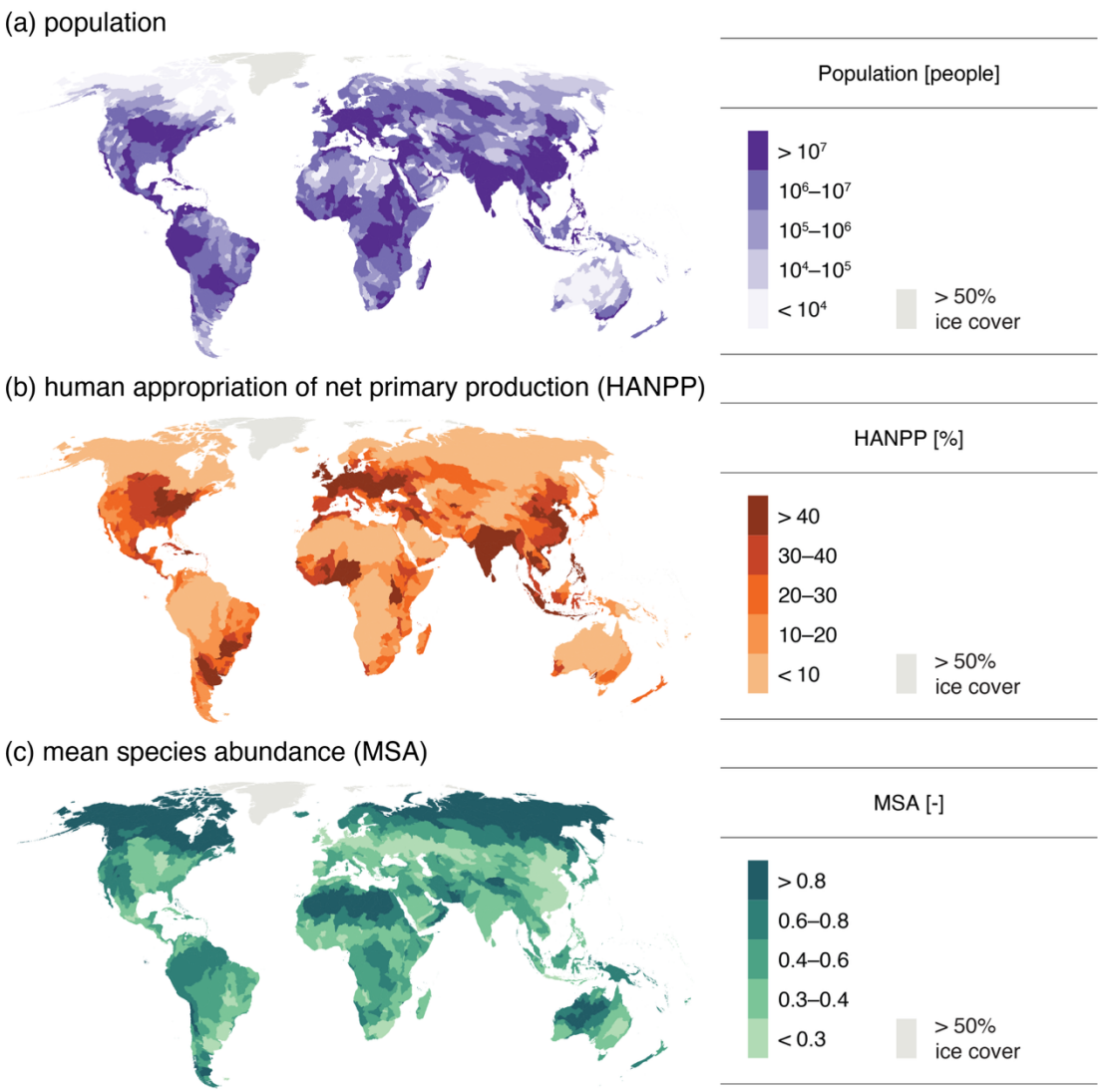

Supplementary Figure 8. Regionally aggregated auxiliary variables. The three auxiliary variables consist of population count[9] (a), human appropriation of net primary production[10] (HANPP) (b), and mean species abundance[11] (MSA) (c). Within each analysed HydroBASINS level 4 catchment[12] (n = 1,268), population count is aggregated with a zonal sum, whereas HANPP and MSA are aggregated with grid cell area weighted zonal averages (Methods). All operations consider only the grid cell fractions that are within the region boundaries[13] and weight the regional sum or average accordingly.

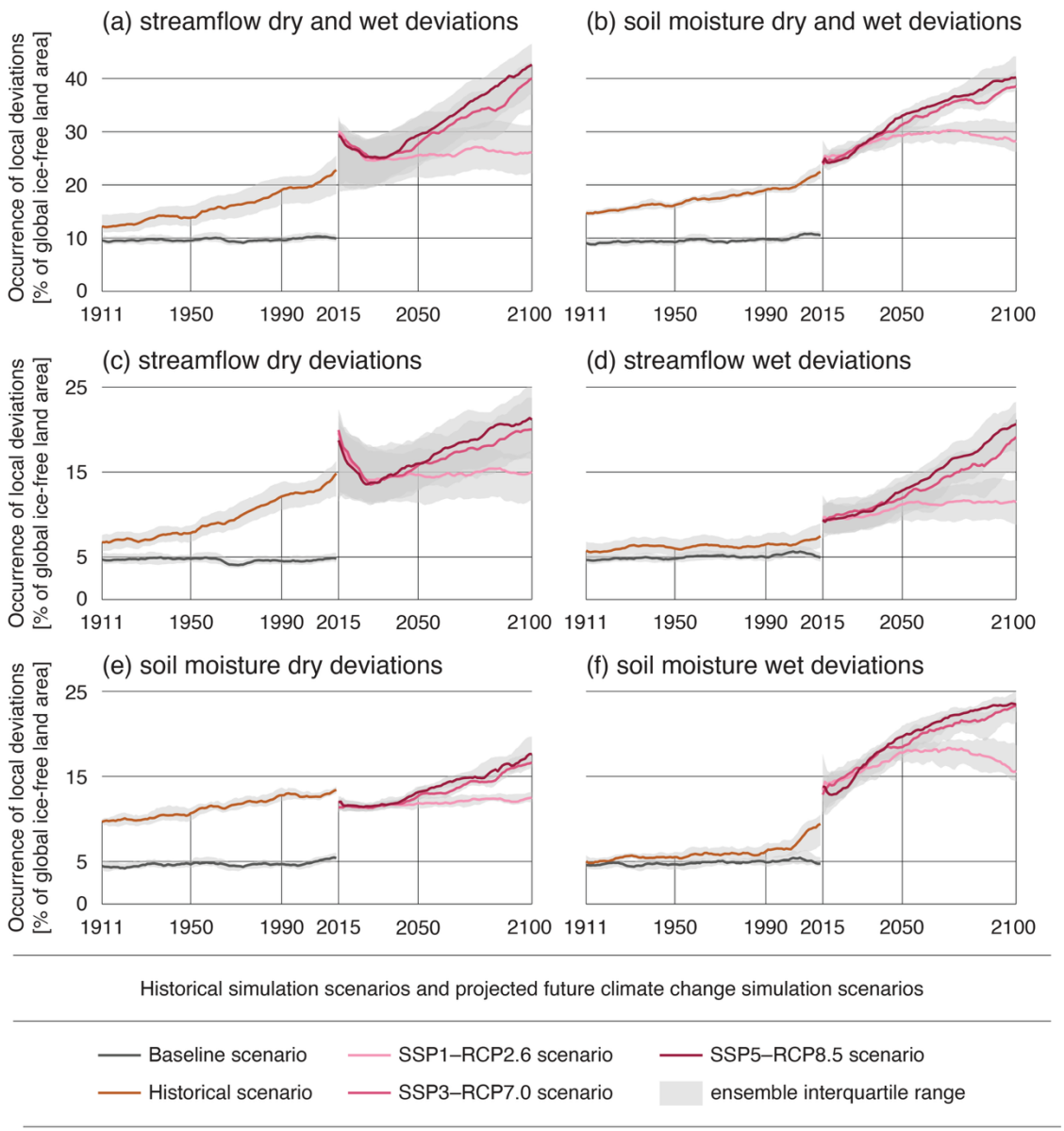

Supplementary Figure 9. Global occurrence of dry and wet local deviations under baseline, historical, and projected future climate change scenarios. The global occurrence of local deviations is measured by the percentage share of global ice-free land area with local deviations, for dry and wet streamflow deviations (a), dry and wet soil moisture deviations (b), dry streamflow deviations (c), wet streamflow deviations (d), dry soil moisture deviations (e), and wet soil moisture deviations (f). Hydrological simulations underlying global deviation occurrence in panels a–f are sourced from Inter-Sectoral Impact Model Intercomparison Project simulation round 3b experiments[2], which re-establishes all scenarios including the baseline scenario (Supplementary Text). Years prior to 1911 are excluded from panels a–f, although used in determining the occurrence of local deviations (Supplementary Text). Shown is the ensemble median of annual percentage, which is computed as an average of monthly percentages. Time series of the occurrence of local deviations and limits of the ensemble interquartile range (IQR) are smoothed with a 10-year moving (trailing) mean over the ensemble median and ensemble IQR limits, respectively.

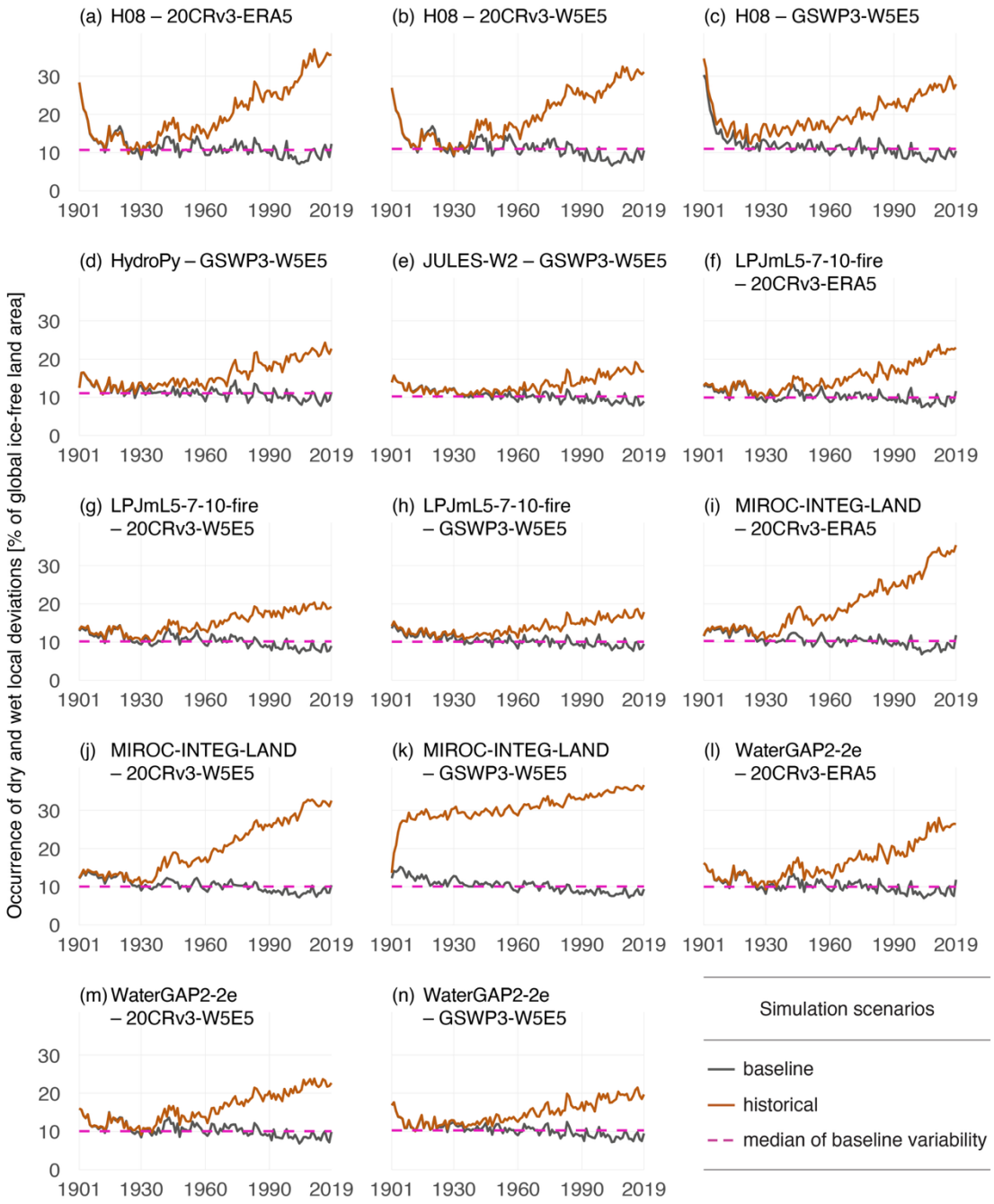

Supplementary Figure 10. Global occurrence of dry and wet local streamflow deviations under baseline and historical scenarios, for each hydrological model ensemble member separately. The global occurrence of local deviations is measured by the percentage share of global ice-free land area with local streamflow deviations, for dry and wet streamflow deviations and for each ensemble member (a–n) (Supplementary Table 2). Shown is the annual percentage, which is computed as an average of monthly percentages (Methods). Time series of the occurrence of local deviations are smoothed with a 10-year moving (trailing) mean over the annual percentage. Although excluded from determining the median of baseline variability, deviation occurrence during years 1901–1910 is shown here to illustrate potential traces of model spinup during the first years of each simulation (Methods).

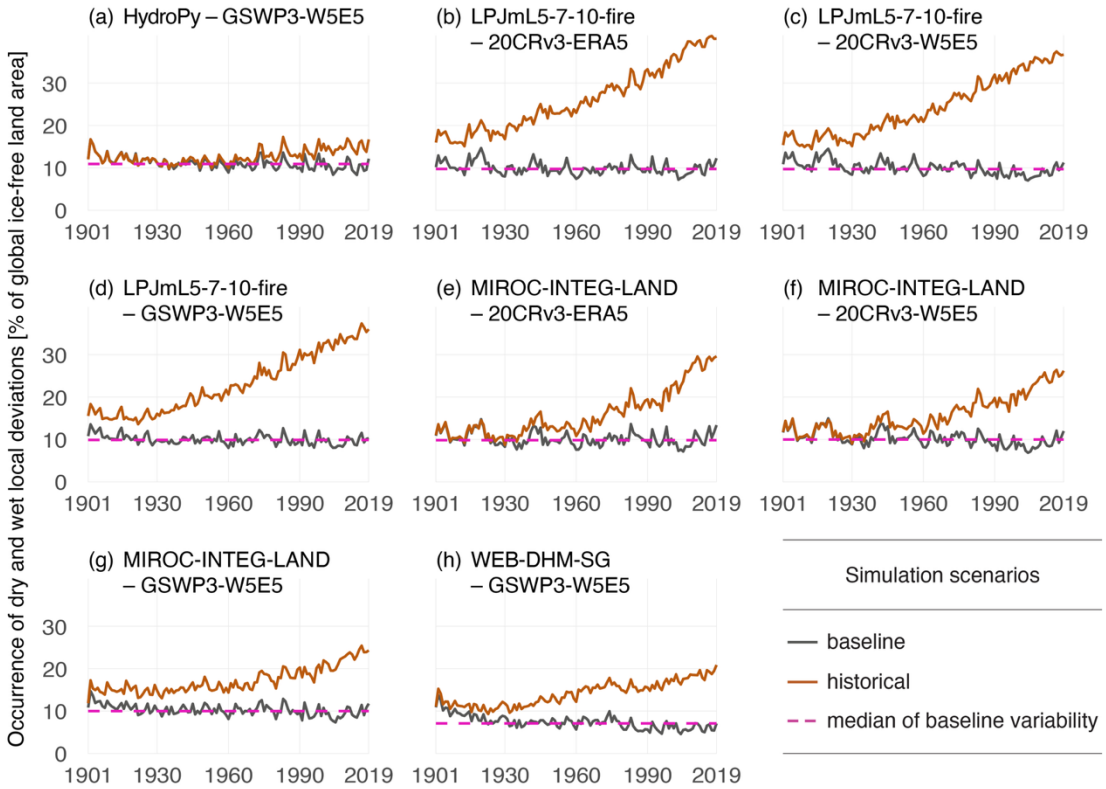

Supplementary Figure 11. Global occurrence of dry and wet local soil moisture deviations under baseline and historical scenarios, for each hydrological model ensemble member separately. The global occurrence of local deviations is measured by the percentage share of global ice-free land area with local soil moisture deviations, for dry and wet soil moisture deviations and for each ensemble member (a–h) (Supplementary Table 2). Shown is the annual percentage, which is computed as an average of monthly percentages (Methods). Time series of the occurrence of local deviations are smoothed with a 10-year moving (trailing) mean over the annual percentage. Although excluded from determining the median of baseline variability, deviation occurrence during years 1901–1910 is shown here to illustrate potential traces of model spinup during the first years of each simulation (Methods).

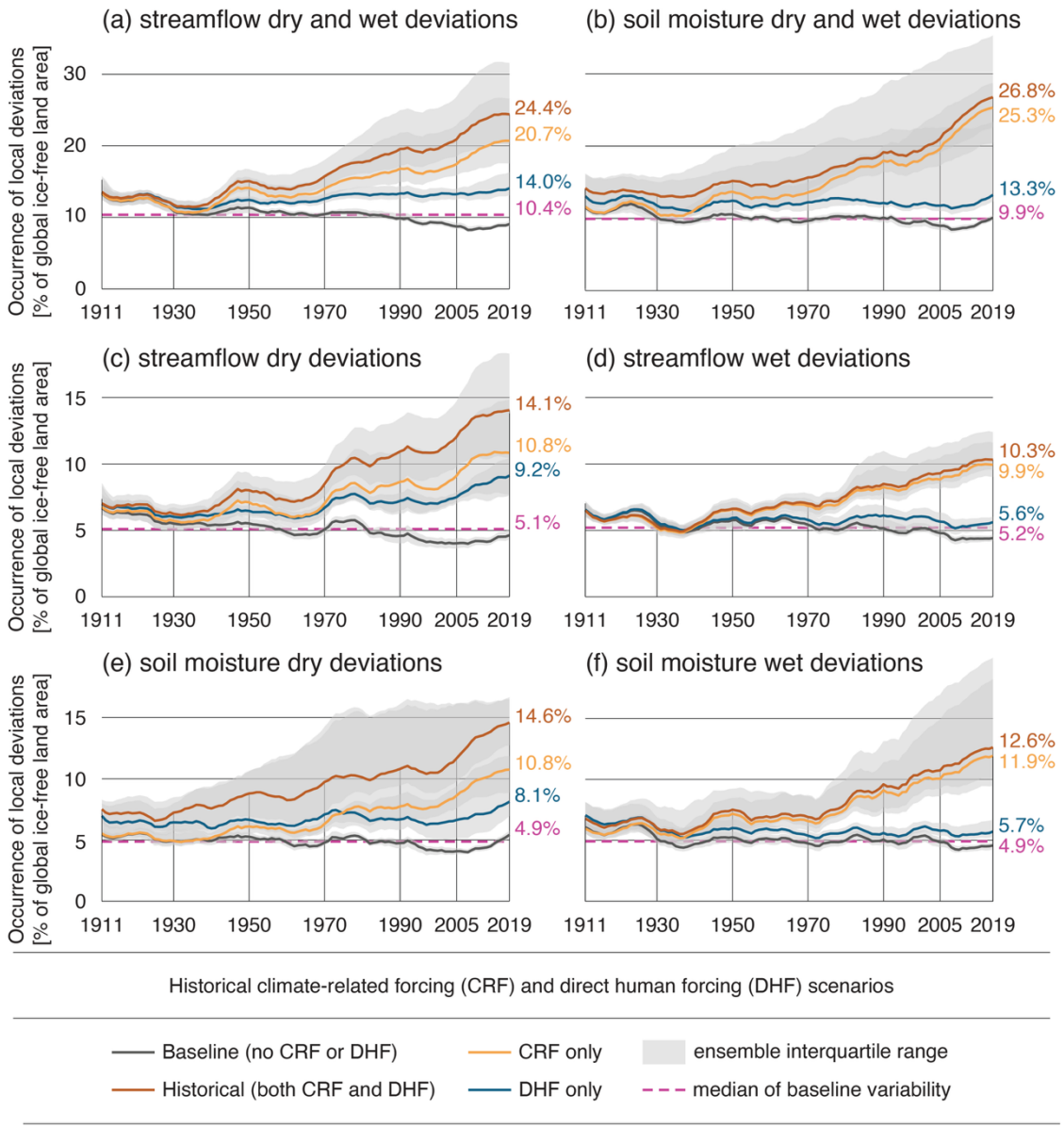

Supplementary Figure 12. Global occurrence of dry and wet local deviations under different climate-related forcing and direct human forcing scenarios, including otherwise excluded ensemble members. The global occurrence of local deviations is measured by the percentage share of global ice-free land area with local deviations, for dry and wet streamflow deviations (a), dry and wet soil moisture deviations (b), dry streamflow deviations (c), wet streamflow deviations (d), dry soil moisture deviations (e), and wet soil moisture deviations (f). Shown is the ensemble median of annual percentage, which is computed as an average of monthly percentages (Methods). Time series of the occurrence of local deviations and limits of the ensemble interquartile range (IQR) are smoothed with a 10-year moving (trailing) mean over the ensemble median and ensemble IQR limits, respectively. When including otherwise excluded ensemble members, the total streamflow data ensemble size becomes n = 14, and the total soil moisture data ensemble size becomes n = 8 (Methods, Supplementary Table 2).

Supplementary Tables

Supplementary Table 1. Group sizes for percentile rank bins synthesising across climate-related forcing (CRF) and direct human forcing (DHF) contributions on regional freshwater deviation occurrence. Global percentile ranks are assigned for scenario contributions in each of the four cases of regional deviation occurrence (streamflow and soil moisture, dry and wet), and the groups (Fig. 6) are created by binning the median of these four ranks for CRF only and DHF only scenarios separately (Methods).

percentile rank bin	group size (CRF only scenario)	group size (DHF only scenario)
[0, 0.2)	2	39
[0.2, 0.4)	155	413
[0.4, 0.6)	864	396
[0.6, 0.8)	232	304
[0.8, 1]	15	116

Supplementary Table 2. Members comprising the global hydrological model (GHM) ensemble (combinations of GHMs and climate-related forcing (CRF) data sets) used in this study. All ensemble members that are available in the Inter-Sectoral Impact Model Intercomparison Project simulation round 3a repository[1,14] with simulations for all desired scenarios are initially selected, and the selection is narrowed down by discarding those ensemble members that are found to mismatch between baseline and historical scenarios in the beginning of the simulation period (Methods).

variable	GHM	CRF data sets for which simulations are available		
		20CRv3-ERA5	20CRv3-W5E5	GSWP3-W5E5
streamflow	H08	x	x	x
streamflow	HydroPy			x
streamflow	JULES-W2			x
streamflow	LPJmL5-7-10-fire	x	x	x
streamflow	MIROC-INTEG-LAND	x	x	x
streamflow	WaterGAP2-2e	x	x	x
soil moisture	HydroPy			x
soil moisture	LPJmL5-7-10-fire	x	x	x
soil moisture	MIROC-INTEG-LAND	x	x	x
soil moisture	WEB-DHM-SG			x

available (included in main results)
available (excluded from main results)
not available

References

1. Frieler, K. *et al.* Scenario setup and forcing data for impact model evaluation and impact attribution within the third round of the Inter-Sectoral Model Intercomparison Project (ISIMIP3a). *Geosci. Model Dev.* **17**, 1–51 (2024).
2. Gosling, S. N. *et al.* ISIMIP3b Simulation Data from the Global Water Sector. ISIMIP Repository https://doi.org/10.48364/ISIMIP.230418.1 (2024).
3. ISIMIP. ISIMIP3b protocol for water_global. https://protocol.isimip.org/#/ISIMIP3b/water_global (2025).
4. Hanasaki, N., Yoshikawa, S., Pokhrel, Y. & Kanae, S. A global hydrological simulation to specify the sources of water used by humans. *Hydrol. Earth Syst. Sci.* **22**, 789–817 (2018).
5. Yokohata, T. *et al.* MIROC-INTEG-LAND version 1: a global biogeochemical land surface model with human water management, crop growth, and land-use change. *Geosci. Model Dev.* **13**, 4713–4747 (2020).
6. Müller Schmied, H. *et al.* The global water resources and use model WaterGAP v2.2e: description and evaluation of modifications and new features. *Geosci. Model Dev.* **17**, 8817–8852 (2024).
7. Lange, S. Trend-preserving bias adjustment and statistical downscaling with ISIMIP3BASD (v1.0). *Geosci. Model Dev.* **12**, 3055–3070 (2019).
8. Porkka, M. *et al.* Notable shifts beyond pre-industrial streamflow and soil moisture conditions transgress the planetary boundary for freshwater change. *Nat. Water* **2**, 262–273 (2024).
9. Klein Goldewijk, K. HYDE data for the Global Carbon Budget (2024). Utrecht University https://doi.org/10.24416/UU01-BV65K3 (2025).
10. Kastner, T. *et al.* Land use intensification increasingly drives the spatiotemporal patterns of the global human appropriation of net primary production in the last century. *Glob. Change Biol.* **28**, 307–322 (2022).
11. Schipper, A. M. *et al.* Projecting terrestrial biodiversity intactness with GLOBIO 4. *Glob. Change Biol.* **26**, 760–771 (2020).
12. Lehner, B. & Grill, G. Global river hydrography and network routing: baseline data and new approaches to study the world's large river systems. *Hydrol. Process.* **27**, 2171–2186 (2013).
13. Baston, D. exactextractr: Fast Extraction from Raster Datasets using Polygons. (2023).
14. Gosling, S. N. *et al.* ISIMIP3a Simulation Data from the Global Water Sector. ISIMIP Repository https://doi.org/10.48364/ISIMIP.398165.5 (2025).